

Aperiodic approximants bridging quasicrystals and modulated structures

Toranosuke Matsubara,¹ Akihisa Koga,¹ Atsushi Takano,² Yushu Matsushita,³ and Tomonari Dotera⁴

¹*Department of Physics, Tokyo Institute of Technology, Meguro, Tokyo 152-8551, Japan*

²*Department of Molecular and Macromolecular Chemistry,
Nagoya University, Nagoya, Aichi 464-8603, Japan*

³*Toyota Physical and Chemical Research Institute, Nagakute, Aichi 480-1192, Japan*

⁴*Department of Physics, Kindai University, Higashi-Osaka, Osaka 577-8502, Japan*

Aperiodic crystals constitute a fascinating class of materials that includes incommensurate (IC) modulated structures [1, 2] and quasicrystals (QCs) [3–8]. Although these two categories share a common foundation in the concept of superspace, the relationship between them has remained enigmatic and largely unexplored. Here, we show “any metallic-mean” QCs [9–11], surpassing the confines of Penrose-like structures, and explore their connection with IC modulated structures. In contrast to periodic approximants of QCs [12, 13], our work introduces the pivotal role of “aperiodic approximants” [14], articulated through a series of k -th metallic-mean tilings serving as aperiodic approximants for the honeycomb crystal, while simultaneously redefining this tiling as a metallic-mean IC modulated structure, highlighting the intricate interplay between these crystallographic phenomena. We extend our findings to real-world applications, discovering these unique tiles in a terpolymer/homopolymer blend [15] and applying our QC theory to a colloidal simulation displaying planar IC structures [16, 17]. In these structures, domain walls are viewed as essential components of a quasicrystal, introducing additional dimensions in superspace. Our research provides a fresh perspective on the intricate world of aperiodic crystals, shedding light on their broader implications for domain wall structures across various fields [18, 19].

Prior to the discovery of quasicrystals (QCs) as the advent of aperiodicity in materials science, incommensurate (IC) modulated structures and IC composite structures were investigated, wherein IC spatial modulations were added to the background crystalline structures [1, 2]. Then, the concept of superspace and additional degrees of freedom known as phasons were introduced. After Shechtman’s discovery [3], aperiodic crystals, including IC modulated structures and QCs, emerged as an important class of materials [4–8]. Aperiodicity is characterized by irrational numbers, thereby making a distinction between the two. In QCs, the irrational numbers are locked by two-length scales [9–11, 20] in geometry, whereas in IC modulated structures, these numbers remain unlocked. QCs typically consist of concentric shell clusters arranged quasiperiodically, locking in the golden mean in icosahedral QCs. In certain alloys, such as Au-Al-Yb [12], periodic approximants are synthesized, where the clusters are arranged periodically. Consequently, “periodic approximants” have been extensively studied to gain a better understanding of QCs. A crucial aspect of periodic approximants is that they exhibit local quasiperiodicity (resembling QCs), but globally display periodicity. Moreover, as the degree of approximation increases, these periodic approximants converge towards QCs [13].

A complementary treatment has been explored where a quasiperiodic structure approaches the periodic one by varying the characteristic irrational. Such treatments are known as “aperiodic approximants” [14]. An elementary example of aperiodic approximants is the generalized Fibonacci sequence, which comprises two letters, A and B . The sequence is generated by the substitution rules: $A \rightarrow AA \cdots AB (= A^k B)$ and $B \rightarrow A$, where k is a natural number. The numbers of the letters A and B at

iteration n ($N_A^{(n)}$ and $N_B^{(n)}$) satisfy

$$\begin{pmatrix} N_A^{(n+1)} \\ N_B^{(n+1)} \end{pmatrix} = \begin{pmatrix} k & 1 \\ 1 & 0 \end{pmatrix} \begin{pmatrix} N_A^{(n)} \\ N_B^{(n)} \end{pmatrix}, \quad (1)$$

where the maximum eigenvalue of the matrix is given by the metallic-mean: $\tau_k = (k + \sqrt{k^2 + 4})/2$. When $k = 1$, the sequence is the conventional Fibonacci one with the golden mean. The eigenvector of the matrix is given by $(\tau_k, 1)^T$, indicating $N_A^{(n)}/N_B^{(n)} \rightarrow \tau_k$ as $n \rightarrow \infty$, where the sequence is filled with the letter A for large values of k . In the limit $k \rightarrow \infty$, the sequence converges to a crystal consisting of consecutive “ A ”s. Hence, the generalized Fibonacci sequence with the metallic-mean can be considered as the aperiodic approximants of the one-dimensional crystal $AAA \cdots$.

Similarly, aperiodic approximants of triangular lattices were proposed. These metallic-mean quasiperiodic tilings start from the bronze-mean tilings [10]. Majority tiles increase with increasing k , and eventually, the systems converge to the triangular lattices in the limit $k \rightarrow \infty$. A crucial aspect of these is that they are locally periodic, but globally quasiperiodic, in other words, they are considered as planar IC modulated structures.

Here we present hexagonal metallic-mean approximants of the honeycomb lattice, which bridge the gap between QCs and IC modulated structures. Schematic of our view is presented in Fig. 1. As the metallic-mean increases, the size of honeycomb domains bounded by the parallelograms also increases, and the whole tiling converges to the honeycomb lattice. Conversely, the metallic-mean IC modulation is introduced to the honeycomb crystals in terms of the metallic-mean tilings. The domain walls composed of parallelograms in the honey-

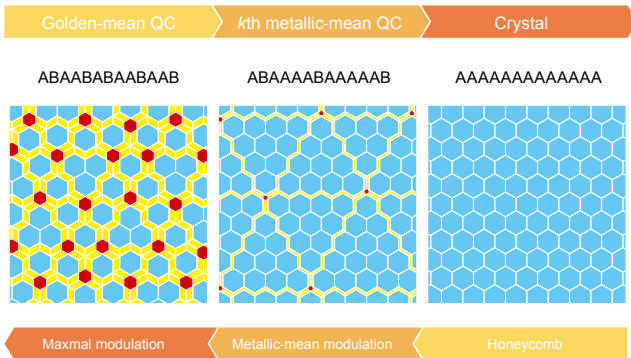


Fig. 1. Aperiodic approximants. Schematic showing the role of aperiodic approximants as a link between quasicrystals and periodic crystals. The link is a series of k -th metallic-mean tilings as an aperiodic approximant of the honeycomb crystal (top arrow), which is simultaneously regarded as a metallic-mean (incommensurate) modulated honeycomb crystal (bottom arrow).

comb crystal are regarded as ingredients of a quasicrystal adding superspace dimensions. Significantly, we show that the metallic-mean tiling scheme is applicable to a polymer system [15] and colloidal systems [16, 17] in soft-matter self-assemblies.

Metallic-mean tilings

We construct the metallic-mean approximants of the honeycomb lattice, which are composed of large hexagons (L), parallelograms (P) and small hexagons (S) shown in Fig. 2a. The ratio between the long (ℓ) and short (s) lengths is given by the metallic-mean $\tau_k (= \ell/s)$. Consequently, the ratio of areas for the three tiles is given by $3\tau_k^2 : \tau_k : 3$. We elaborate the substitution rules for these tiles as a natural extension of those for the hexagonal golden-mean tiling [11] (Fig. 2b). The substitution rules for $k = 2$ and $k = 3$ are illustrated in Figs. 2c and 2d, respectively. Notice that the matching rule of the tilings are introduced by solid and open circles. When the deflation rule is applied to an L tile, an S tile is generated at the center of the original L tile, thereby, six zig-zag chains of P tiles emanate from the central S tile, which is clearly found in the case with $k = 3$. The rest region is filled by L tiles. Upon one deflation process, a P tile is changed to one P tile and L tiles, and an S tile is changed to one L tile. Hence, one can construct the substitution rules of three tiles for any k , which are subjected to the substitution rule for the generalized Fibonacci sequence: $\ell \rightarrow \ell^k s$ and $s \rightarrow \ell$. See also Supplementary Fig. 1 showing how these rules are extended to the cases of $k = 4$ and $k = 5$.

Two-dimensional space is covered without gaps after iterative deflation processes, as shown in Figs. 2e-g and Supplementary Fig. 2 for $k = 1 - 5$. Because of the deflation process, self-similarity is an inherent property of the metallic-mean tilings: Supplementary Fig. 3 exem-

plifies exact self-similarity for $k = 2$ and $k = 3$. We find that a finite number of adjacent L tiles are bounded by the P tiles, which can be regarded as an isolated ‘‘honeycomb domain’’. For examples, in the case with $k = 2$, the domains are composed of one, three, or six L tiles, as shown in Fig. 2f. We confirm that each honeycomb domain bounded by the P tiles is composed of a_{k-1}, a_k , or a_{k+1} adjacent L tiles in the k th metallic-mean tiling, where $a_k = k(k+1)/2$, see Supplementary Note 3. Therefore, increasing k , the number of the L tiles in each honeycomb domain quadratically increases. On the other hand, the S and P tiles are located around the corners and edges of the honeycomb domains, and thereby their numbers should be $O(1)$ and $O(k)$, respectively. These suggest that the L tiles become majority in the large k case and the single honeycomb domain is realized in the limit $k \rightarrow \infty$, as shown in Fig. 2h. Using a deflation matrix described in Method, it is easy to evaluate the frequencies of tiles (f_L, f_P , and f_S) and the ratio of the corresponding areas (S_L, S_P , and S_S) rendered in Fig. 2i and its inset. For $k = 5$, more than ninety percent of the two-dimensional space is occupied by L tiles. See Method in details.

The tiling has eight unique types of vertices as shown in Fig. 3a classified by their coordination numbers and their circumstances. The frequency of each type can be exactly computed, and the explicit formulae for any k are presented in Supplementary Note 2. Figure 3b shows the frequencies of the vertex types as a function of k . As expected, the frequencies of the C_0 and C_1 vertices monotonically increase and approach $1/2$ implying the convergence to the honeycomb lattice.

The metallic-mean tilings are bipartite since they are composed of hexagons and parallelograms. As shown in Fig. 3a, the vertex types C_1 - C_3 belong to the A sublattice and the others belong to the B sublattice, as depicted by open and solid circles, respectively. We find that the sublattice imbalance in the system given as $\Delta = f_A - f_B = 1/(3 + \sqrt{k^2 + 4})$, where $f_A (= f_{C_1} + f_{C_2} + f_{C_3})$ and $f_B (= f_{C_0} + f_{D_0} + f_{D_1} + f_E + f_F)$ are the fractions of the A and B sublattices, respectively. This distinct property is in contrast to those for the bipartite Penrose, Ammann-Beenker, and Socolar dodecagonal tilings where each type of vertices equally belongs to both sublattices [21].

As shown in Fig. 3c, we can distinguish two kinds of L tiles denoted by L_Δ and L_∇ , introducing up and down triangles located at their centers so that three corners of each triangle point the filled circles on the vertices of the L tile. In Fig. 3d, we find the following properties: (1) Two kinds of honeycomb domains composed of L_Δ or L_∇ tiles are alternatively arranged. (2) The shape of L_Δ domains is up-triangular and that of L_∇ domains is down-triangular. (3) Domain walls are composed of consecutive zigzag P tiles. (4) Three domain walls should meet at a point of S hexagons. (5) Intervals between domain walls are not periodic, but metallic-mean incommensurately modulated, as shown in Method and Sup-

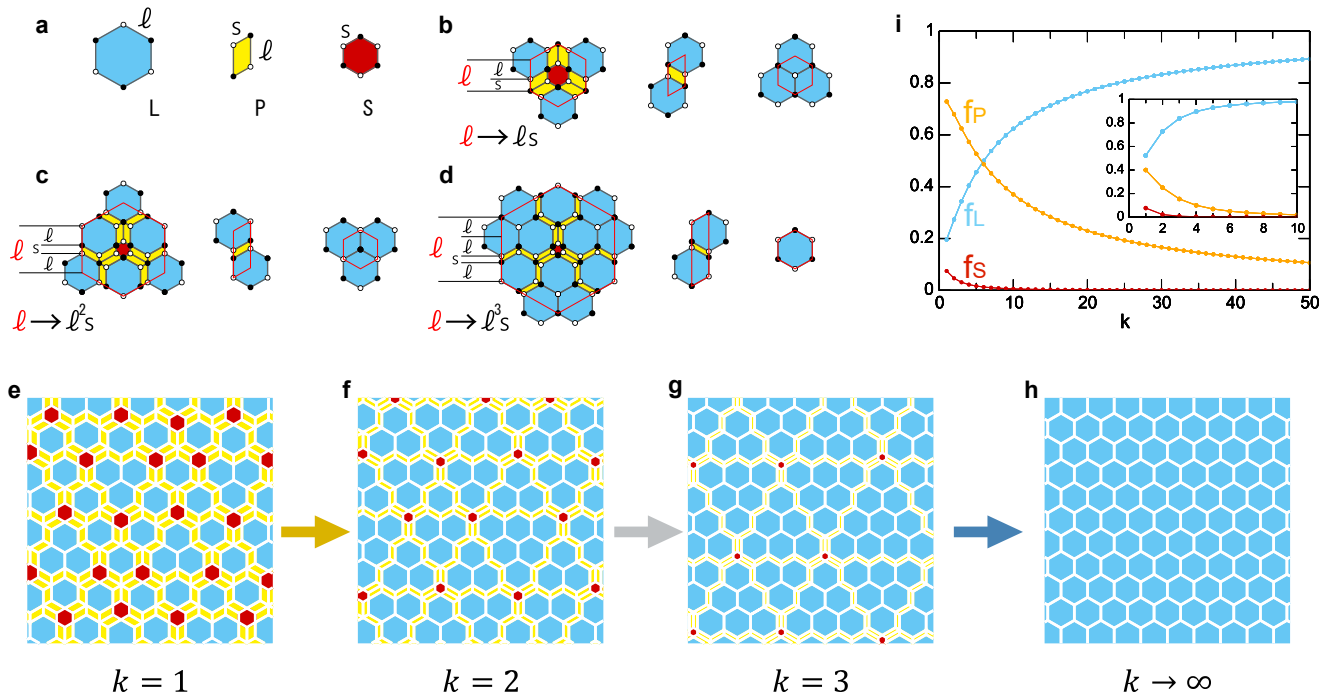


Fig. 2. Metallic-mean tilings. **a**, Large hexagons (L), parallelograms (P) and small hexagons (S) with edge lengths ℓ and s . Vertices are decorated with open and solid circles alternatively to introduce the matching rule of the tiling. **b-d**, Substitution rules for the golden-mean tiling ($k = 1$)(b), silver-mean tiling ($k = 2$)(c), and bronze-mean tiling ($k = 3$)(d). **e**, Golden-mean tiling. **f**, Silver-mean tiling. **g**, Bronze-mean tiling. **h**, Honeycomb lattice. **i**, Frequencies of L, P, and S tiles as a function of k , and the corresponding fraction for each area (inset). The convergence to the periodic honeycomb lattice is assessed.

plementary Fig. 6.

Superspace representation

To provide a theoretical basis for the metallic-mean tilings, we construct their higher-dimensional description. In this powerful method, the superspace is divided into the physical space and its complement, known as the perpendicular space. A tiling is viewed as a projection of a hypercubic crystal in the superspace onto the two-dimensional physical space. The projections onto the perpendicular space are densely filled in specific areas, as illustrated in Fig. 3f, which are referred to as windows. These windows are derived from sections perpendicular to the threefold axis of a rhombohedron (octahedron) that is the projection of the hypercubic unit cell, showcasing hexagonal and triangular shapes in Extended Data Fig. 1. The figure also highlights the regions associated with the eight vertex types, as detailed in the Method section and Supplementary Fig. 8.

Application to soft matter

The metallic-mean tilings are physical entities in two soft-matter systems. We consider self-assembled crystalline structures obtained in soft materials with the P31m plane group, as illustrated in Fig. 4a, which belongs to the two-dimensional hexagonal Bravais lattice but lacks hexago-

nal rotational axes. Further crystallographic description is given in Supplementary Notes 8 and 9 for colloidal particles and polymer blends, respectively.

The first application of the metallic-mean tiling is a polymer system reported by Izumi *et al.*, who found a complex ordered structure in an ABC triblock terpolymer/homopolymer blend system [15]. Sample preparation is provided in Method. Figure 4b illustrates the decoration of L, P, and S tiles by three kinds of polymers. In the previous study, regular large domains consisting of only L tiles were observed. It is noticed that the triangle inside a hexagon has two directions, up and down. In the present study, we searched samples again and found P tiles in a TEM picture rendered in Fig. 4c. In Fig. 4c, a regular region of an extended L_{∇} area in the center and a domain wall represented by a row of zigzag P tiles on the left-hand side. We can interpret the rows of P tiles within the L sea as twin boundaries, which mark a transition between different crystal orientations, L_{Δ} and L_{∇} . It's worth emphasizing that a row of P tiles physically changes the crystal orientations, demonstrating the tangible properties of P tiles beyond mathematical concepts. We note that the decoration of S tile (Fig. 4b) is hypothetical and it has not been observed in the samples.

The second application of the metallic-mean tiling is a

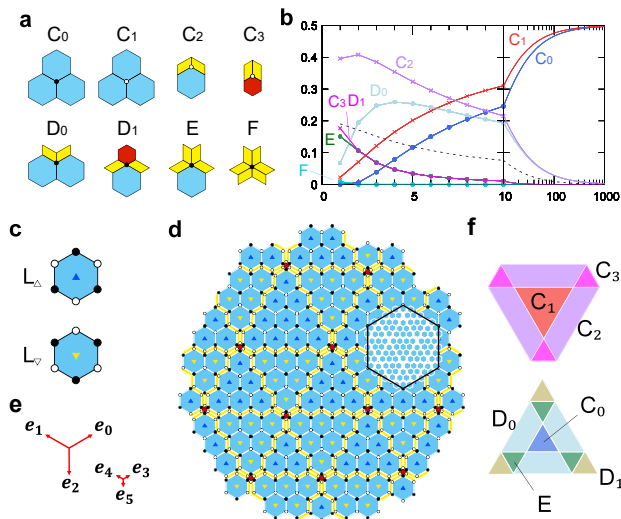


Fig. 3. Vertex types. Vertices are alternatively decorated with the open and solid circles to define A and B sublattices, respectively. **a**, Eight types of vertices. **b**, Frequencies of the vertex types. Dashed line represents the sublattice imbalance Δ . **c**, Two kinds of the L tiles, L_{Δ} and L_{∇} . **d**, Honeycomb domain structures for the hexagonal bronze-mean tilings. L_{Δ} tiles form up-triangular domains, and L_{∇} tiles form down-triangular domains. **e**, Projected basis vectors e_i ($i = 0, \dots, 5$) from fundamental translation vectors in six dimensions. **f**, Windows in the perpendicular space. Each area shows the vertex types.

colloidal particle simulation in two dimensions conducted by Engel [16]. It utilizes a Lennard-Jones–Gauss (LJG) potential [22] that has two distinct length scales. In Method, we have reproduced his result. We find that the LJG particles occupy the same positions as the dark gray circles in Figs. 4a–c. Moreover, in Fig. 2 of the Engel’s paper and his Supplementary Figure S1 in particular, it was shown to form twin-boundary superstructures on a scale much larger than the potential range: the size of superstructures depends on the temperature reversibly; the lower the temperature, the larger the size. One finds that regular L_{Δ} or L_{∇} domains form triangle shapes of several sizes, which property is also characteristic of the metallic-mean tiling. Additionally, it was observed that twin boundaries only intersect at triple junctions, which situation mimics the metallic-mean tilings, where triple rows consisting of the P tiles meet at the location of an S hexagon, though the correspondence between the P tiles and domain walls in the LJG system is not always exact. Nonetheless, the metallic-mean scheme mimics Engel’s modulated superstructures with changing scale ratios or k values.

In Fig. 4d, an ideal decoration model for the particle system generated by the higher-dimensional quasicrystal theory with the 5-th metallic-mean modulation (Supplementary Note 12). In these cases, as shown in Figs. 4e and 4f, the structure factor $S(\mathbf{q}) = \left| \frac{1}{N} \sum_i e^{i\mathbf{q} \cdot \mathbf{r}_i} \right|^2$ theoretically calculated in terms of the superspace represen-

tation dramatically reproduces the numerical FFT for the diffraction images shown in Fig. 3 of the Engel’s paper. As clearly shown in the magnified views (Fig. 4f), the prominent peaks appear at almost the same positions, while the aperiodic modulation of the metallic-mean tiling yields the satellite peaks in the vicinity of the main peaks, which is the characteristic property of IC structures.

Discussion

Our previous study has covered the multiples-of-3 metallic-means, through the hexagonal aperiodic approximants of the triangular lattice [14]. The present work broadens the scope of aperiodic approximants. Firstly, our tiling serves as the approximant of the honeycomb lattice. Secondly, it enables an inflation ratio of *any* metallic-mean, thereby enhancing the applicability.

In fact, we have applied the tiling concept to explore real materials, such as polymer and colloidal systems. Our analysis successfully identifies large hexagons as regular structures and parallelograms as twin boundaries. It is noted that similar IC triangular domain structures were discovered in quartz and aluminum phosphate long time ago [18, 19], known as Dauphiné twins in trigonal quartz. We surmise that there is a similar mechanism behind the formation.

We emphasize that the decorated perpendicular space windows in 6D generate the 2D IC structures, whose method has been developed in the field of QC studies. It is striking that the satellite peaks can be calculated not by direct real-space Fourier transform, but by perpendicular-space Fourier transform of the windows. By comparing these peaks with those observed in two-dimensionally IC modulated structures, we establish a foundation for analysis of IC structures in terms of the QC methodology.

One of the origins of the P31m plane group demonstrated here is the aggregation tendency of pentagons. Regular pentagons cannot tile the entire plane without gaps, as shown by Dürer–Kepler–Penrose, however, there are pentagon-related tilings if we abort five-fold symmetry. In Supplementary Note 10, we demonstrate the accommodation of pentagons within both a square and a hexagon. Using 4-fold symmetry, the Cairo pentagonal tiling and its dual, *i.e.*, the $3^2.4.3.4$ Archimedean tiling with the P4gm have been considered [23]. The latter Archimedean tiling is associated with the σ phase found in complex metallic and soft-matter phases, which is recognized as a periodic approximant of dodecagonal QCs [24–29]. It is noteworthy that P31m plane group structure is a 3-fold variant of the Cairo tiling and the σ phase.

Our study highlights the effectiveness of aperiodic approximants in inducing modulations within self-assembled soft-matter systems employing the P31m plane group. Specifically, we utilized the rows of P tiles as domain boundaries in the honeycomb lattice, thereby bridging metallic-mean hexagonal QCs and IC modu-

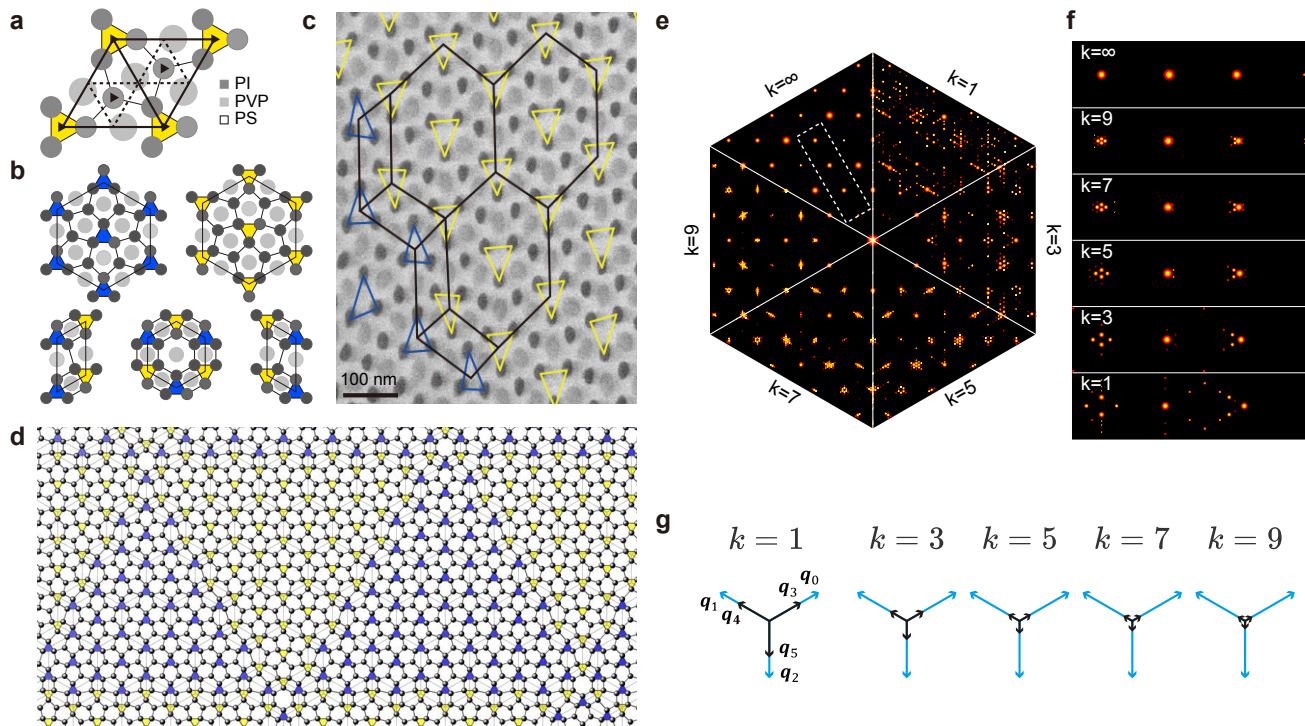


Fig. 4. Application to soft matter. **a**, Diagram of the P31m plane group. **b**, Schematic decoration of L, P, and S tiles by ABC triblock terpolymer/homopolymer blend ISP-III/S. Dark gray circles indicate polyisoprene (PI), light gray circles indicate poly(2-vinylpyridine) (PVP), and the other matrix region is polystyrene (PS). **c**, TEM image from the ABC triblock terpolymer/homopolymer ISP-III/S. **d**, Ideal particle decoration for a colloidal system generated by the 5-th metallic-mean tiling. Up and down triangles form blue and yellow triangular domains reproducing colloidal simulations. **e**, Each sector shows the structure factor for the decorated k -th metallic-mean tiling when $k = 1, 3, 5, 7, 9$, and ∞ . **f**, Magnified views of slices of the structure factor indicated by a dashed rectangle in **e**. In the vicinity of main peaks, the aperiodic modulation yields satellite peaks characterizing IC structures. **g**, Six reciprocal vectors \mathbf{q}_i ($i = 0, 1, \dots, 5$) for $k = 1, 3, 5, 7, 9$.

lated honeycomb lattices. The dynamic movement of domain walls while maintaining triple junctions can be explained by the phason flips of L, S, and P tiles, as illustrated in Extended Data Fig. 3 and Supplementary Note 4. In this context, the colloidal system appears to be a phason-random tiling version of the metallic-mean tiling

system. Lastly, applying the deterministic growth rules, known as OSDS rules [30], reveals that dead surfaces consist of these domain walls. Overall, our research offers a fresh perspective, providing novel insights into the realm of both aperiodic crystals and their broader implications for domain wall structures across various fields.

-
- [1] de Wolff, P., Janssen, T. & Janner, A. The superspace groups for incommensurate crystal structures with a one-dimensional modulation. *Acta Cryst. A* **37**, 625–636 (1981).
- [2] Bak, P. Commensurate phases, incommensurate phases and the devil’s staircase. *Rep. Prog. Phys.* **45**, 587–629 (1982).
- [3] Shechtman, D., Blech, I., Gratias, D. & Cahn, J. W. Metallic phase with long-range orientational order and no translational symmetry. *Phys. Rev. Lett.* **53**, 1951 (1984).
- [4] Penrose, R. The role of aesthetics in pure and applied mathematical research. *Bull. Inst. Math. Appl.* **10**, 266–271 (1974).
- [5] Levine, D. & Steinhardt, P. J. Quasicrystals: A new class of ordered structures. *Phys. Rev. Lett.* **53**, 2477–2480 (1984).
- [6] Janssen, T., Chapuis, G. & de Boissieu, M. *Aperiodic Crystals: From Modulated Phases to Quasicrystals* (Oxford University Press, Oxford, 2007).
- [7] Janssen, T. & Janner, A. Aperiodic crystals and superspace concepts. *Acta Cryst. B* **70**, 617–651 (2014).
- [8] de Boissieu, M., Janssen, T. & Janner, A. Aperiodic crystals. *Acta Cryst. A* **75**, 273–280 (2019).
- [9] Beenker, F. P. M. Algebraic theory of non-periodic tilings of the plane by two simple building blocks: a square and a rhombus. *EUT report. WSK, Dept. of Mathematics and Computing Science* **82-WSK-04** (1982).
- [10] Dotera, T., Bekku, S. & Zihlerl, P. Bronze-mean hexagonal quasicrystal. *Nat. Mat.* **16**, 987–992 (2017).

- [11] Coates, S. *et al.* Hexagonal and trigonal quasiperiodic tilings. *arXiv preprint arXiv:2201.11848* (2023).
- [12] Deguchi, K. *et al.* Quantum critical state in a magnetic quasicrystal. *Nat. Mat.* **11**, 1013–1016 (2012).
- [13] Goldman, A. I. & Kelton, R. F. Quasicrystals and crystalline approximants. *Rev. Mod. Phys.* **65**, 213–230 (1993).
- [14] Nakakura, J., Zihlerl, P., Matsuzawa, J. & Dotera, T. Metallic-mean quasicrystals as aperiodic approximants of periodic crystals. *Nat. Comm.* **10**, 4235 (2019).
- [15] Izumi, Y., Yamada, M., Takano, A. & Matsushita, Y. A new periodic pattern with five-neighbored domain packing from abc triblock terpolymer/b homopolymer blend. *J. Polym. Sci. Part B, Polym. Phys.* **53**, 907–911 (2015).
- [16] Engel, M. Entropic stabilization of tunable planar modulated superstructures. *Phys. Rev. Lett.* **106**, 095504 (2011).
- [17] Schoberth, H. G. *et al.* Molecular dynamics study of colloidal quasicrystals. *Soft Matter* **12**, 7644–7654 (2016).
- [18] van Tendeloo, G., van Landuyt, J. & Amelinckx, S. The $\alpha \rightarrow \beta$ phase transition in quartz and alpo4 as studied by electron microscopy and diffraction. *Phys. Status Solidi (a)* **33**, 723–735 (1976).
- [19] Van Landuyt, J., Van Tendeloo, S., G. and Amelinckx & Walker, M. B. Interpretation of dauphiné-twin-domain configurations resulting from the $\alpha - \beta$ phase transition in quartz and aluminum phosphate. *Phys. Rev. B* **31**, 2986–2992 (1985).
- [20] Dotera, T., Oshiro, T. & Zihlerl, P. Mosaic two-lengthscale quasicrystals. *Nature* **506**, 208–211 (2014).
- [21] Koga, A. & Tsunetsugu, H. Antiferromagnetic order in the hubbard model on the penrose lattice. *Phys. Rev. B* **96**, 214402 (2017).
- [22] Engel, M. & Trebin, H.-R. Self-assembly of monatomic complex crystals and quasicrystals with a double-well interaction potential. *Phys. Rev. Lett.* **98**, 225505 (2007).
- [23] Takano, A. *et al.* A mesoscopic archimedean tiling having a new complexity in an abc star polymer. *J. Polym. Sci. Part B, Polym. Phys.* **43**, 2427–2432 (2005).
- [24] Zeng, X. *et al.* Supramolecular dendritic liquid quasicrystals. *Nature* **428**, 157–160 (2004).
- [25] Talapin, D. *et al.* Quasicrystalline order in self-assembled binary nanoparticle superlattices. *Nature* **461**, 964–967 (2009).
- [26] Iacovella, C. R., Keys, A. S. & Glotzer, S. C. Self-assembly of soft-matter quasicrystals and their approximants. *Proc Natl Acad Sci USA* **108**, 20935–20940 (2011).
- [27] Xiao, C., Fujita, N., Miyasaka, K., Sakamoto, Y. & Terasaki, O. Dodecagonal tiling in mesoporous silica. *Nature* **487**, 349–353 (2012).
- [28] Zhang, J. & Bates, F. S. Dodecagonal quasicrystalline morphology in a poly(styrene-b-isoprene-b-styrene-b-ethylene oxide) tetrablock terpolymer. *J. Am. Chem. Soc.* **134**, 7636–7639 (2012).
- [29] Förster, S., Meinel, K., Hammer, R., Trautmann, M. & Widdra, W. Quasicrystalline structure formation in a classical crystalline thin-film system. *Nature* **502**, 215–218 (2013).
- [30] Onoda, G. Y., Steinhardt, P. J., DiVincenzo, D. P. & Socolar, J. E. S. Growing perfect quasicrystals. *Phys. Rev. Lett.* **60**, 2653–2656 (1988).

Methods

Deflation matrix of the metallic-mean tiling

The metallic-mean tilings are regarded as the aperiodic approximants of the honeycomb lattice. To discuss quantitatively how the metallic-mean tilings approach the honeycomb lattice with increasing k , we construct the deflation matrix. At each deflation process, the increase of the numbers of L, P, and S tiles is explicitly given by $\mathbf{v}_{n+1} = M\mathbf{v}_n$ with $\mathbf{v}_n = (N_L^{(n)} N_P^{(n)} N_S^{(n)})^T$ and

$$M = \begin{pmatrix} k^2 & k & 1 \\ 6k & 1 & 0 \\ 1 & 0 & 0 \end{pmatrix}, \quad (2)$$

where $N_\alpha^{(n)}$ is the number of the tile α , which stands for L, P, or S at iteration n . The maximum eigenvalue of the matrix M is τ_k^2 , and the corresponding eigenvector is given as $(\tau_k^2 \ 6\tau_k \ 1)^T$. We evaluate the frequencies for these tiles in the large k limit approach $f_L = \tau_k^2/Z$, $f_P = 6\tau_k/Z$, $f_S = 1/Z$, where $Z = \tau_k^2 + 6\tau_k + 1$. The k -dependent frequencies for three tiles are shown in Fig. 2i. Increasing k , the frequency of the L tiles monotonically increases and approaches unity.

Domain boundaries

The domain boundaries composed of consecutive zig-zag P tiles intersect at small hexagons and pass through the opposite edge of the small hexagons with keeping alternating directions of P tiles. If we ignore these slithering configuration of P tiles, there are three sets of parallel domain walls, as displayed in Fig. 3d. Focusing on a set of parallel domain walls, we observe two types of intervals between the domain walls denoted by \mathcal{S}_S and \mathcal{S}_L , as shown in Supplementary Fig. 6 for silver- and bronze-mean tilings. There are intriguing properties for the intervals. First, for the k -th metallic-mean tilings, the interval \mathcal{S}_S and \mathcal{S}_L consists of k and $k+1$ consecutive L tiles. Second, upon the deflation, we find the substitution rules: $\mathcal{S}_L \rightarrow \mathcal{S}_L^{\frac{1}{2}} \mathcal{S}_S^k \mathcal{S}_L^{\frac{1}{2}}$, and $\mathcal{S}_S \rightarrow \mathcal{S}_L^{\frac{1}{2}} \mathcal{S}_S^{k-1} \mathcal{S}_L^{\frac{1}{2}}$. The numbers of intervals $N_{\mathcal{S}_S}^{(n)}$ and $N_{\mathcal{S}_L}^{(n)}$ of the n -th generation satisfy

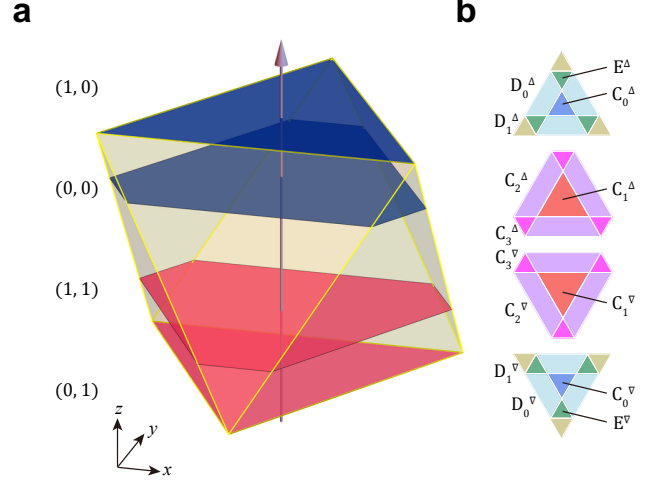
$$\begin{pmatrix} N_{\mathcal{S}_S}^{(n+1)} \\ N_{\mathcal{S}_L}^{(n+1)} \end{pmatrix} = \begin{pmatrix} k-1 & k \\ 1 & 1 \end{pmatrix} \begin{pmatrix} N_{\mathcal{S}_S}^{(n)} \\ N_{\mathcal{S}_L}^{(n)} \end{pmatrix}, \quad (3)$$

where the maximum eigenvalue of the matrix is given by the metallic-mean τ_k . The eigenvector of the matrix is given by $(\tau_k - 1/\tau_k, 1 + 1/\tau_k)^T$, indicating $N_{\mathcal{S}_S}^{(n)}/N_{\mathcal{S}_L}^{(n)} \rightarrow \tau_k$ as $n \rightarrow \infty$, where the sequence is filled with \mathcal{S}_S intervals for large k values. Therefore, we conclude that the intervals between domain walls are metallic-mean modulated.

Superspace representation

We outline main steps of the construction of the metallic-mean tiling by projection of a higher-dimensional hyperlattice onto the physical space. Let ℓ and s be the lengths

of the long and short edges of the tiling. We here assume that the ratio $\eta = s/\ell$ is a variable to apply the tiling to soft-matter systems, while the ratio in the perpendicular space is set to be $1/\tau_k$ to keep the arrangement of the metallic-mean tiling. When $\eta = 1/\tau_k$, the tiling is the exact self-similar metallic-mean tiling generated by the deflation rules.



Extended Data Fig. 1. **Superspace perspective.** **a**, the perpendicular space for the bronze-mean tiling. **b**, Four windows on the right-hand side are obtained from a regular octahedron (middle part of a rhombohedron) of edge length $\sqrt{3}(1 + \tau_k^{-1})$. The top (1,0) and bottom (0,1) windows are equilateral triangular faces of the solid, and hexagonal windows indicated by (0,0) and (1,1) are the sections of the octahedron. In the solid, blue and red colors correspond to honeycomb domains with L_Δ and L_∇ , respectively. In each window, each color corresponds to the vertex type rendered in Fig. 3b.

Each vertex site in the tiling is described by a six-dimensional lattice point $\vec{n} = (n_0, n_1, \dots, n_5)^T$, labeled with integers n_m . Let the six-dimensional lattice point \vec{r}^h in the six-dimensional space \mathcal{S}^h as $\vec{r}^h = R\vec{n}$:

$$R = \begin{pmatrix} \ell c_6 & -\ell c_6 & 0 & s c_6 & -s c_6 & 0 \\ \ell s_6 & \ell s_6 & -\ell & s s_6 & s s_6 & -s \\ \tau_k^{-1} c_6 & -\tau_k^{-1} c_6 & 0 & -c_6 & c_6 & 0 \\ \tau_k^{-1} s_6 & \tau_k^{-1} s_6 & -\tau_k^{-1} & -s_6 & -s_6 & 1 \\ \sqrt{2}\tau_k^{-1} & \sqrt{2}\tau_k^{-1} & \sqrt{2}\tau_k^{-1} & 0 & 0 & 0 \\ 0 & 0 & 0 & -\sqrt{2} & -\sqrt{2} & -\sqrt{2} \end{pmatrix}, \quad (4)$$

where R is the mapping matrix and $c_6 = \cos(\pi/6)$, $s_6 = \sin(\pi/6)$. Namely, the matrix is represented by the six-dimensional basis vectors \vec{e}_i^h ($i = 0, 1, \dots, 5$): $(\vec{e}_i^h)_j = R_{ji}$. The vertex site \mathbf{r} in the physical space \mathcal{S} is given by the first two components of the vector: $\mathbf{r} = ((\vec{r}^h)_0, (\vec{r}^h)_1) = \sum_{m=0}^5 n_m \mathbf{e}_m$, where the projected vectors of the form $\mathbf{e}_m = (R_{0m}, R_{1m})$ with lengths ℓ and s are displayed in Fig. 3e. The remaining four-dimensional perpendicular space is split into two-dimensional spaces $\tilde{\mathcal{S}}$ and \mathcal{S}^\perp , and the corresponding coordinates $\tilde{\mathbf{r}}$ and \mathbf{r}^\perp are given as $\tilde{\mathbf{r}} = ((\vec{r}^h)_2, (\vec{r}^h)_3) = \sum_{m=0}^5 n_m \tilde{\mathbf{e}}_m$, $\mathbf{r}^\perp = ((\vec{r}^h)_4, (\vec{r}^h)_5) = \sum_{m=0}^5 n_m \mathbf{e}_m^\perp$, where $\tilde{\mathbf{e}}_m = (R_{2m}, R_{3m})$ and $\mathbf{e}_m^\perp = (R_{4m}, R_{5m})$.

Note that $\tilde{\mathbf{r}}$ points are densely filled on four planes with $\mathbf{r}^\perp = \{(\sqrt{2}\tau_k^{-1}, 0), (0, 0), (\sqrt{2}\tau_k^{-1}, -\sqrt{2}), (0, -\sqrt{2})\}$ denoted by $\{(1,0), (0,0), (1,1), (0,1)\}$, having polygonal windows shown in Extended Data Fig. 1. Notice that the windows are faces and sections for a regular octahedron. This octahedron is the middle part of a rhombohedron of edge length $\sqrt{3}(1 + \tau_k^{-1})$, which is the projection of the hypercubic unit cell. In Extended Data Figure 1, $\tilde{\mathbf{r}}$ is plotted in the (x, y) -directions, while for \mathbf{r}^\perp both $(\tilde{r}^h)_4$ and $(\tilde{r}^h)_5$ are projected onto the z component. We find that in the limit $k \rightarrow \infty$, the upper and lower hexagons get closer to the top and bottom faces, respectively, and finally they become the equilateral triangles. The explicit sizes of hexagonal windows are presented in Supplementary Fig. 8.

The six-dimensional reciprocal lattice vectors $\tilde{\mathbf{q}}_i^h$ are defined to have the following property $\tilde{\mathbf{e}}_i^h \cdot \tilde{\mathbf{q}}_j^h = 2\pi\delta_{ij}$ with δ_{ij} is the Kronecker delta. It is easy to find $(\tilde{\mathbf{q}}_j^h)_i = Q_{ij}$, where $RQ^T = 2\pi\delta_{ij}$ and

$$Q = C \begin{pmatrix} c_6 & -c_6 & 0 & \tau_k^{-1}c_6 & -\tau_k^{-1}c_6 & 0 \\ s_6 & s_6 & -1 & \tau_k^{-1}s_6 & \tau_k^{-1}s_6 & -\tau_k^{-1} \\ sc_6 & -sc_6 & 0 & -lc_6 & lc_6 & 0 \\ ss_6 & ss_6 & -s & -ls_6 & -ls_6 & l \\ \psi & \psi & \psi & 0 & 0 & 0 \\ 0 & 0 & 0 & -\psi\tau_k^{-1} & -\psi\tau_k^{-1} & -\psi\tau_k^{-1} \end{pmatrix} \quad (5)$$

with $C = 4\pi/[3(\ell + s\tau_k^{-1})]$ and $\psi = (\ell\tau_k + s)/(2\sqrt{2})$. $\mathbf{q} = ((\tilde{\mathbf{q}}_i^h)_0, (\tilde{\mathbf{q}}_i^h)_1) = \sum_{m=0}^5 n_m \mathbf{q}_m$, where the projected vectors $\mathbf{q}_m = (Q_{0m}, Q_{1m})$ with lengths $1/\ell$ and $1/(\ell\tau_k)$ are displayed in Fig. 4g. The remaining four-dimensional perpendicular space is split into two-dimensional reciprocal spaces and the corresponding reciprocal vectors $\tilde{\mathbf{q}}$ and \mathbf{q}^\perp are given as $\tilde{\mathbf{q}} = ((\tilde{\mathbf{q}}_i^h)_2, (\tilde{\mathbf{q}}_i^h)_3) = \sum_{m=0}^5 n_m \tilde{\mathbf{q}}_m$, $\mathbf{q}^\perp = ((\tilde{\mathbf{q}}_i^h)_4, (\tilde{\mathbf{q}}_i^h)_5) = \sum_{m=0}^5 n_m \mathbf{q}_m^\perp$, where $\tilde{\mathbf{q}}_m = (Q_{2m}, Q_{3m})$ and $\mathbf{q}_m^\perp = (Q_{4m}, Q_{5m})$. The detailed procedure is given in Supplementary Note 5.

When computing the Fourier transforms, we rely on the following identity for any pair of vectors in the superspace lattice $\tilde{\mathbf{r}}^h$ and in the corresponding reciprocal lattice $\tilde{\mathbf{q}}^h$: $1 = \exp(i\tilde{\mathbf{q}}^h \cdot \tilde{\mathbf{r}}^h) = \exp(i\mathbf{q} \cdot \mathbf{x}) \exp(i\tilde{\mathbf{q}} \cdot \tilde{\mathbf{x}}) \exp(i\mathbf{q}^\perp \cdot \mathbf{x}^\perp)$. If particle's positions are described by δ -functions so that the density reads $f(\mathbf{r}) = \sum_{j=1}^N \delta(\mathbf{r} - \mathbf{r}_j)$, then the Fourier transform of the density is calculated as

$$\int d\mathbf{r} e^{-i\mathbf{q} \cdot \mathbf{r}} f(\mathbf{r}) = \sum_{j=1}^N e^{-i\mathbf{q} \cdot \mathbf{x}_j} = \sum_{j=1}^N e^{i\tilde{\mathbf{q}} \cdot \tilde{\mathbf{x}}_j} e^{i\mathbf{q}^\perp \cdot \mathbf{x}_j^\perp},$$

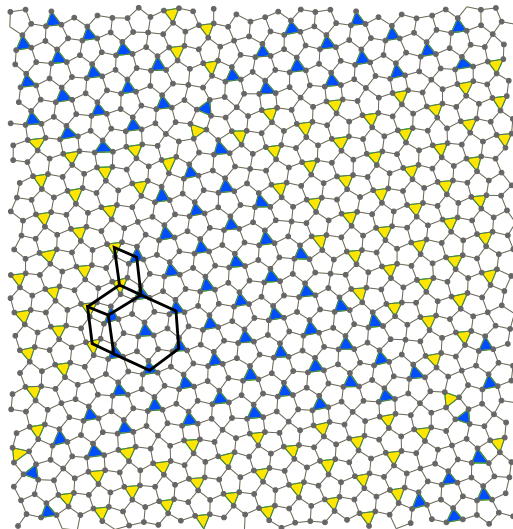
in the last step, we resorted to the above identity.

To construct decorated tilings (Fig. 4d) for soft-matter systems, we set $\eta = s/\ell = 0.6249$. In this case, we employ sections of a rhombohedron as extensional windows. Detailed procedures are presented in Supplementary Notes 8 and 12.

Polymer details

An ISP (I: polyisoprene, S: polystyrene, P: poly(2-vinylpyridine)) triblock terpolymer sample was prepared by a sequential monomer addition technique of an anionic polymerization from cumyl-potassium as an initiator in tetrahydrofuran (THF), while styrene homopolymer was synthesized anionically with *sec*-butyllithium in benzene. The average molecular weight of the terpolymer is 161k and the composition is $\phi_I/\phi_S/\phi_P = 0.25/0.53/0.22$, whereas that of the styrene homopolymer is 9k. The

overall composition of the blend sample is $\phi_I/\phi_S/\phi_P = 0.17/0.68/0.15$, where polystyrene block/styrene homopolymer ratio of $w_S(b)/w_S(h) = 1.4$. The sample film was obtained by casting for two weeks from a dilute solution of THF followed by heating at 150°C for two days. The specimens for morphological observation were cut by an ultramicrotome of Leica model Ultracut UCT into ultrathin sections of about 100 nm thickness and stained with OsO₄ for the TEM observation. Further details are provided in the previous reference [15].



Extended Data Fig. 2. **Colloidal simulation.** Monte Carlo simulation for the Lennard-Jones-Gauss potential at $T = 0.270$.

Simulations of colloidal particles

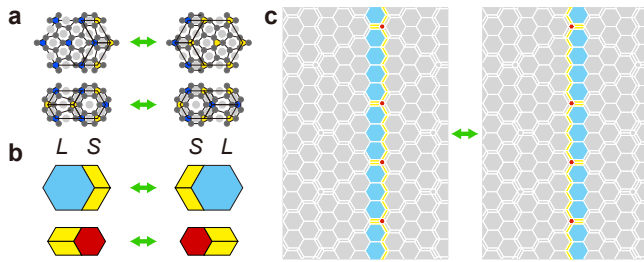
We used *NPT* Monte Carlo simulations of $N = 10000$ colloidal particles interacting with the Lennard-Jones-Gauss potential [16, 22] given by

$$V(r) = \frac{1}{r^{12}} - \frac{2}{r^6} - \epsilon \exp\left(-\frac{(r - r_0)^2}{2\sigma^2}\right), \quad (6)$$

with parameters $\sigma^2 = 0.042$, $\epsilon = 1.8$, $r_0 = 1.42$ at $T = 0.270$, $P = 0.0$. There are slight differences between simulations (Extended Data Fig. 2) and the metallic-mean tiling model (Fig. 4): (1) Dynamically, P tiles are not always perfect. (2) There are five particles in an S tile in simulations, while six particles in the latter. The effect of these is negligible in the structure factor. Further data including diffraction images is provided in Supplementary Note 11.

Phasons

Domain walls dynamically move with keeping triple junctions can be explained by the phason flips of L, S and P tiles, as shown in Extended Data Fig. 3. In this sense, the colloidal system appears to be a phason-random tiling version of the metallic-mean tiling system. The existence and the conservation of S tiles in the phason flips is the key of triple junctions of domain walls at moderate thermal excitations. See also Supplementary Note 4.



Extended Data Fig. 3. **Phason flips.** **a**, Schematic phason move in self-assembled pattern from ABC triblock terpolymer/homopolymer blend. **b**, Two types of phason flips in the metallic-mean tiling. **c**, Move of a twin boundary by a row of phason flips.

Data availability

The whole datasets are available from the corresponding author on reasonable request.

Code availability

The codes used to construct the tilings and the projection windows are available from the corresponding author on reasonable request.

Acknowledgements

The authors thank M. Engel, M. Mihalkovic, and P. Ziherl for valuable discussions. Parts of the numerical calculations are performed in the supercomputing systems in ISSP, the University of Tokyo. This work was supported by Grant-in-Aid for Scientific Research from JSPS, KAKENHI Grant Nos. JP22K03525, JP21H01025, JP19H05821 (A.K.).

Author contributions

T.M. & A.K. proposed the tiling theory. T.D. developed the application to soft matter. A.T. & Y.M. conducted polymer experiments. T.M., A.K. & T.D. wrote the manuscript.

Additional information

Supplementary Information accompanies this paper at <http://XXX>.

Competing interests: The authors declare no competing interests.

Reprints and permission information is available online at <http://npg.nature.com/reprintsandpermissions/>

Publisher's note: Springer Nature remains neutral with regard to jurisdictional claims in published maps and institutional affiliations.

Correspondence and requests for materials should be addressed to A. K. (email: koga@phys.titech.ac.jp) and T. D. (email: dotera@phys.kindai.ac.jp).

Aperiodic approximants bridging quasicrystals and modulated structures

Toranosuke Matsubara,¹ Akihisa Koga,¹ Atsushi Takano,² Yushu Matsushita,³ and Tomonari Dotera⁴

¹*Department of Physics, Tokyo Institute of Technology, Meguro, Tokyo 152-8551, Japan*

²*Department of Molecular and Macromolecular Chemistry,
Nagoya University, Nagoya, Aichi 464-8603, Japan*

³*Toyota Physical and Chemical Research Institute, Nagakute, Aichi 480-1192, Japan*

⁴*Department of Physics, Kindai University, Higashi-Osaka, Osaka 577-8502, Japan*

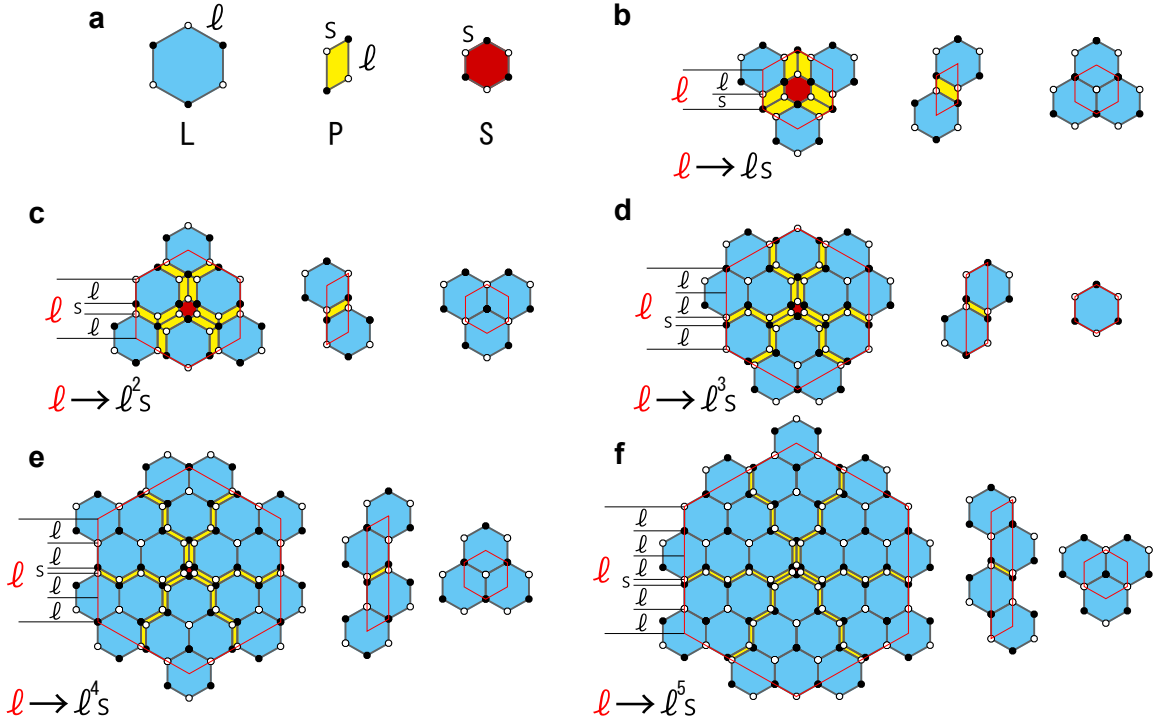
(Dated: March 26, 2024)

Contents

1. Substitution rules for the hexagonal metallic-mean tilings	1
2. Fractions of the vertices	3
3. Honeycomb domain	5
4. Domain boundaries	7
5. Higher-dimensional representation	8
6. Phason flips	13
7. Lattice structure factors	15
8. Crystallographic description of the P31m particle system	17
9. Crystallographic description of the P31m polymer blend system	19
10. Pentagon tilings	20
11. Colloidal system	21
12. Atomic decorations	22
References	27

Supplementary Note 1 Substitution rules for the hexagonal metallic-mean tilings

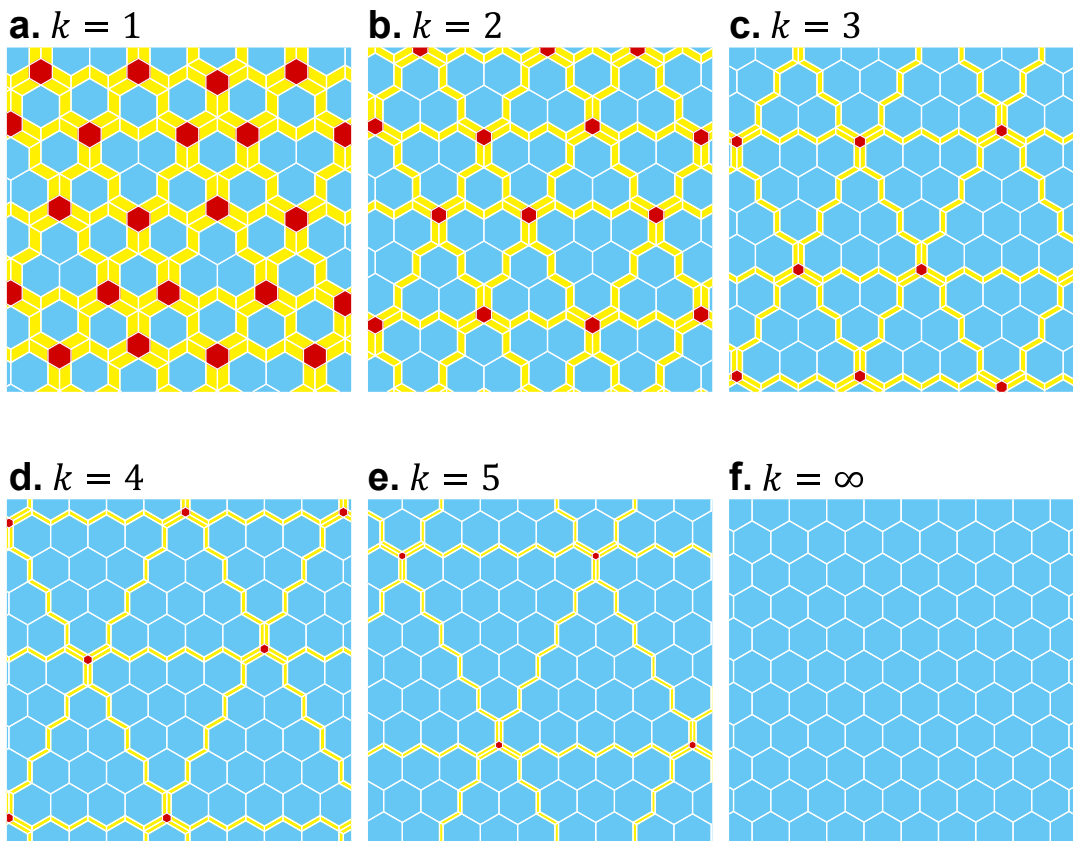
The hexagonal metallic-mean tiling we propose in the main text is composed of large hexagons (L), parallelograms (P), and small hexagons (S). The length ratio is given by the metallic mean τ_k , with $\tau_k = (k + \sqrt{k^2 + 4})/2$. Extending the rule for the hexagonal golden-mean tiling¹, we propose the substitution rules for the metallic-mean tilings, which are explicitly shown in Supplementary Fig. 1. When the deflation rule is applied to an L tile, an S tile is generated



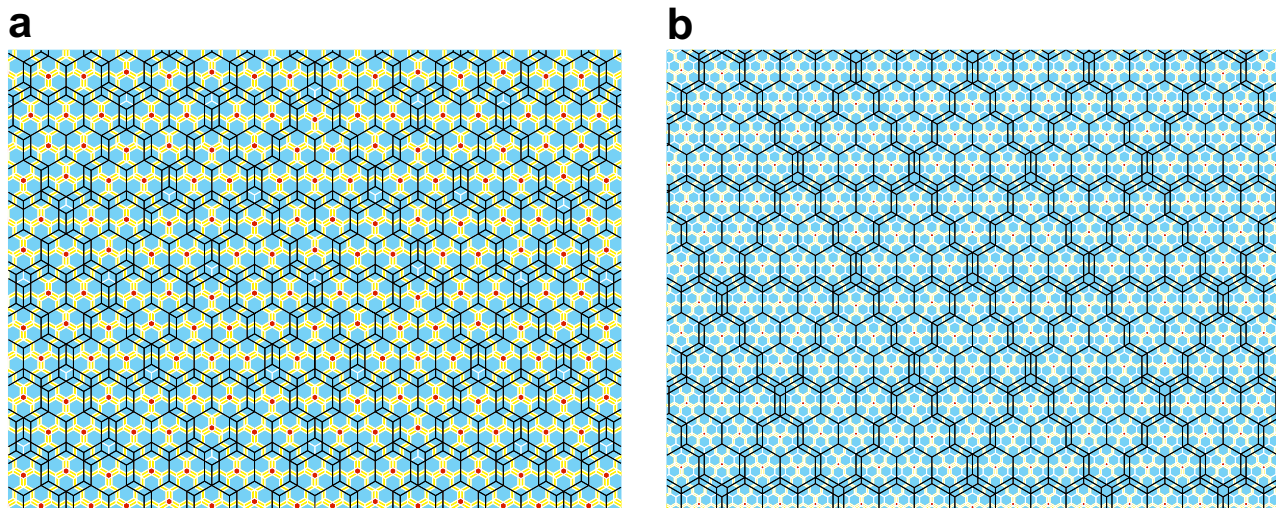
Supplementary Fig. 1. **a** Large hexagon, parallelogram, and small hexagon. **b-f** Substitution rules for the golden-mean, silver-mean, bronze-mean, 4th metallic-mean, and 5th metallic-mean tilings.

at the center of the original L tile. Furthermore, six chains sharing a short edge of k P tiles are adjacent to the S tile and are located along six directions $(\cos \pi i/3, \sin \pi i/3)$ ($i = 0, 1, \dots, 5$). The rest region is filled by k^2 L tiles. As for a P tile, $k/3$ L tiles are generated along the longer edge of the original P tile, and one P tile is generated around the center. Note that there are two kinds of the P tiles: a P tile shown in Supplementary Fig. 1a and its reflected tile (\bar{P} tile). We find that the P (\bar{P}) tile appears for odd (even) k case when the substitution rule is applied to a P tile. An S tile is replaced to one L tile under one deflation operation. We find the triple periodicity in k for the deflation process of the S tile. These allow us to generalize the substitution rules for any metallic-mean tilings.

We obtain the hexagonal metallic-mean tilings, applying the substitution rule to a certain tile iteratively. The metallic-mean tilings for $k = 1, 2, 3, 4, 5$, and the honeycomb lattice, which can be regarded as the tiling with $k \rightarrow \infty$, are shown in Supplementary Fig. 2. When one deflation operation is applied to the tilings, the number of tiles increases and the self-similar structure appears, which are shown in Supplementary Figs. 3a and 3b.



Supplementary Fig. 2. Hexagonal metallic-mean tilings. **a** Golden-mean tiling ($k = 1$)¹, **b** silver-mean tiling ($k = 2$) and **c** bronze-mean tiling ($k = 3$). **d** and **e** represent metallic-mean tilings with $k = 4$ and $k = 5$. **f** represents the honeycomb lattice with $k \rightarrow \infty$.



Supplementary Fig. 3. Self-similarity of hexagonal metallic-mean tilings. **a** Silver-mean tiling. **b** Bronze-mean tiling. The colored tilings are obtained by applying the deflation operation to the tilings shown as the black lines.

Supplementary Note 2 Fractions of the vertices

We derive the fractions of vertices for $k \neq 1$ (the fractions for $k = 1$ have been given in Ref¹). In the case of $k \neq 1$, we could not find the F vertex shared by six P tiles ($f_F = 0$). This is because vertices shared by two adjacent P tiles are always shared by the L or S tile according to the substitution rules for $k \neq 1$, as shown in Supplementary Figs. 1c-1f. When one evaluates the fractions for certain graphs such as vertices and domains, it is convenient to consider the ratio between numbers of tiles and vertices for the hexagonal metallic-mean tiling in the thermodynamic limit. Supplementary Figure 1a clearly shows that the net numbers of sites in L, P, and S tiles are two, one, and two, respectively. Therefore, we obtain the ratio r_k as

$$r_k = 2f_L + f_P + 2f_S = \frac{P_k}{\tau_k^2 + 6\tau_k + 1}, \quad (1)$$

where $P_k = 2\tau_k^2 + 6\tau_k + 2$. We first focus on the bipartite structure. The sublattice structures for the L, P, and S tiles are shown as the open and solid circles in Supplementary Fig. 1a, where these are referred to as A and B sublattices. By counting the net numbers of the site belonging to each sublattice in L, P, and S tiles, we obtain its fractions as,

$$f_A = \frac{1}{r_k} \left(f_L + \frac{2}{3}f_P + f_S \right) = \frac{1}{2} + \frac{\tau_k}{P_k}, \quad (2)$$

$$f_B = \frac{1}{r_k} \left(f_L + \frac{1}{3}f_P + f_S \right) = \frac{1}{2} - \frac{\tau_k}{P_k}. \quad (3)$$

This naturally leads to the sublattice imbalance in the hexagonal metallic-mean tilings,

$$\Delta = f_A - f_B = \frac{1}{3 + \sqrt{k^2 + 4}}. \quad (4)$$

Since the sublattice A (B) is composed of C_1 , C_2 , and C_3 (C_0 , D_0 , D_1 , and E) vertices, we obtain the following equations,

$$f_A = f_{C_1} + f_{C_2} + f_{C_3}, \quad (5)$$

$$f_B = f_{C_0} + f_{D_0} + f_{D_1} + f_E. \quad (6)$$

In the tilings, two adjacent tiles share the edge, which is connected between the neighboring sites in A and B sublattices. Therefore, we obtain the equations for the total number of longer and shorter edges,

$$3f_{C_1} + 2f_{C_2} + f_{C_3} = 3f_{C_0} + 3f_{D_0} + 2f_{D_1} + 3f_E, \quad (7)$$

$$f_{C_2} + 2f_{C_3} = f_{D_0} + 2f_{D_1} + 2f_E, \quad (8)$$

where the left (right) hand side of the equations represents the total number of edges, which is expressed by the numbers of vertices belonging to the A (B) sublattice. According to the substitution rule, the C_3 , D_1 , and E vertices always appear around the S tile for $k \neq 1$. Therefore, these fractions are then given as

$$f_{C_3} = f_{D_1} = f_E = \frac{3f_S}{r_k} = \frac{3}{P_k}. \quad (9)$$

From these equations, we obtain the exact fractions of vertices in the hexagonal metallic-mean tilings as

$$f_{C_0} = \begin{cases} 0 & (k = 1) \\ \frac{1}{2} - \frac{7}{4\tau_k} + \frac{1}{2P_k}(27 - 7k) & (k \neq 1) \end{cases}, \quad (10)$$

$$f_{C_1} = \frac{1}{2} - \frac{5}{4\tau_k} + \frac{5}{2P_k}(3 - k), \quad (11)$$

$$f_{C_2} = \frac{3}{2\tau_k} - \frac{3}{P_k}(4 - k), \quad (12)$$

$$f_{C_3} = \frac{3}{P_k}, \quad (13)$$

$$f_{D_0} = \begin{cases} \frac{3}{4\tau_1^5} & (k = 1) \\ \frac{3}{2\tau_k} - \frac{3}{P_k}(6 - k) & (k \neq 1) \end{cases}, \quad (14)$$

$$f_{D_1} = \frac{3}{P_k}, \quad (15)$$

$$f_E = \begin{cases} \frac{3\sqrt{5}}{4\tau_1^5} & (k = 1) \\ \frac{3}{P_k} & (k \neq 1) \end{cases}, \quad (16)$$

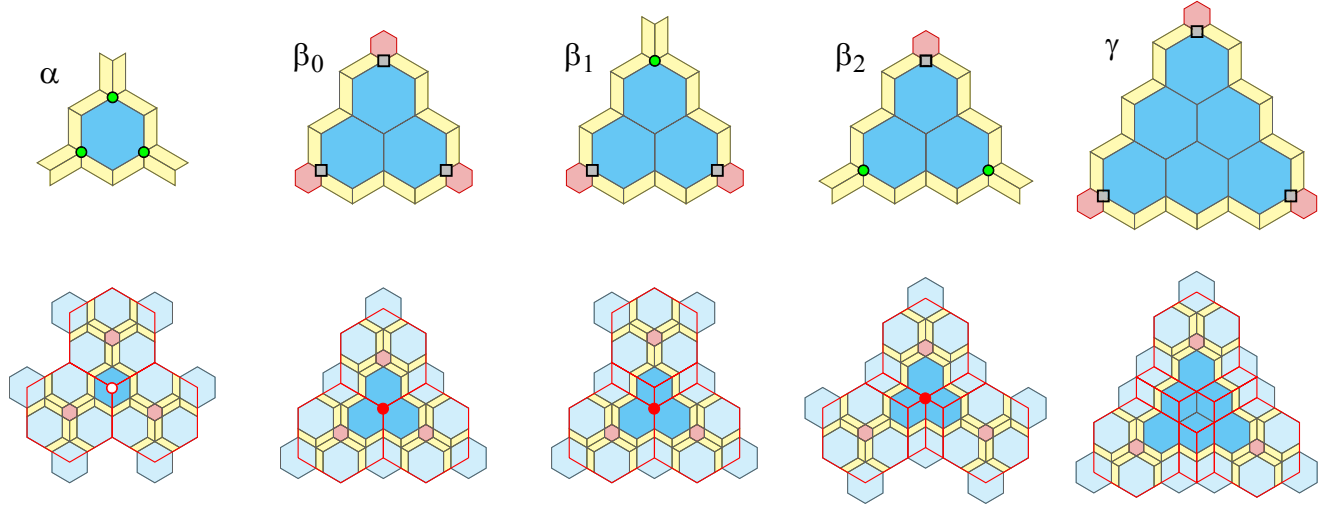
$$f_F = \begin{cases} \frac{1}{4\tau_1^7} & (k = 1) \\ 0 & (k \neq 1) \end{cases}. \quad (17)$$

The average of the coordination number is given by

$$\begin{aligned} z_k &= 3 \sum_i f_{C_i} + 4 \sum_i f_{D_i} + 5f_E + 6f_F \\ &= 3 + \frac{3}{2\tau_k} + \frac{3(k-3)}{P_k}. \end{aligned} \quad (18)$$

In the hexagonal metallic-mean tilings, the average of the coordination number depends on k . $z_k \rightarrow 3$ when the system approaches the honeycomb lattice $k \rightarrow \infty$.

Supplementary Note 3 Honeycomb domain



Supplementary Fig. 4. Upper panels: $\alpha, \beta_0, \beta_1, \beta_2$, and γ domains in the hexagonal silver-mean tiling, which are bounded by some P and S tiles. Circles and squares indicate E and D_1 vertices at the corners of the honeycomb domains. Lower panels: the red lines represent the results of the inflation operation applied to the tiles around the honeycomb domains shown in the upper panels. Red open (solid) circles at the vertices indicate the A (B) sublattice in the inflated tiling.

Here, we focus on the honeycomb domain in the hexagonal metallic-mean tilings with $k \neq 1$, which is composed of finite number of the L tiles and is bounded by the P and S tiles. As seen in Supplementary Fig. 2, in the hexagonal metallic-mean tiling with $k \neq 1$, there exist three kinds of domains composed of a_{k-1}, a_k or a_{k+1} L tiles, where $a_k = k(k+1)/2$. These are referred to as α, β and γ domains. Supplementary Figure 4 shows α, β , and γ domains in the silver-mean tilings, as an example. We find that in the α domain, the E vertex shared by one L tile and four P tiles, which is shown as the circle, is located at each corner site. In the γ domain, the D_1 vertex shared by one L tile, two P tiles and one S tile, which is shown as the square, is located at each corner site. On the other hand, the β domains can be divided into the $\beta_i (i = 0, 1, 2)$ domains, where i E vertices and $(3-i)$ D_1 vertices are located at three corner sites, as shown in Supplementary Fig. 4. The absence of the β_3 domains will be proved below.

To examine the fraction of each domain, we consider the substitution rule for the tiles. In the lower panels of Supplementary Fig. 4, we show the tiling structure obtained by the inflation operation as the red lines. We find that the C_1, C_0, D_0, E vertices, and S tiles generated by an inflation operation are located at the center of the $\alpha, \beta_0, \beta_1, \beta_2$, and γ domains. Therefore, we obtain the following equations as

$$f_\alpha = \frac{r_k f_{C_1}}{\tau_k^2}, \quad (19)$$

$$f_{\beta_0} = \frac{r_k f_{C_0}}{\tau_k^2}, \quad (20)$$

$$f_{\beta_1} = \frac{r_k f_{D_0}}{\tau_k^2}, \quad (21)$$

$$f_{\beta_2} = \frac{r_k f_E}{\tau_k^2}, \quad (22)$$

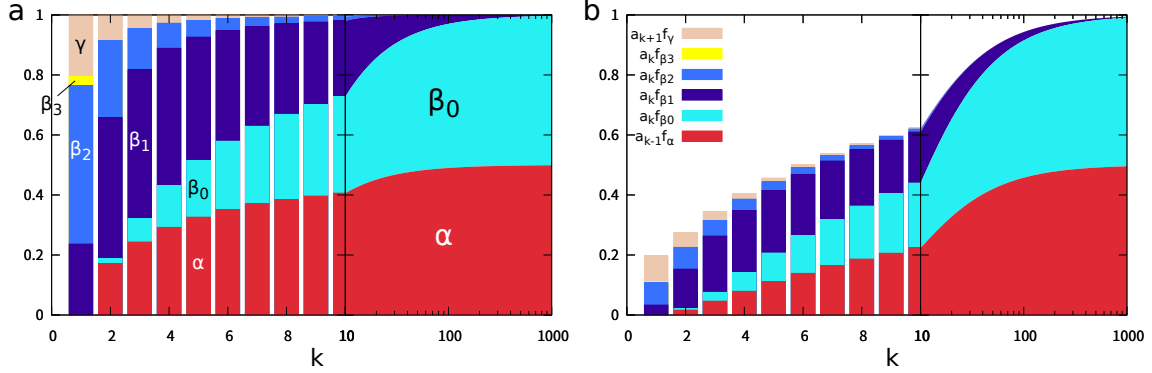
$$f_\gamma = \frac{f_S}{\tau_k^2}, \quad (23)$$

where f_X is the ratio of the number of $X (= \alpha, \beta_i, \gamma)$ domains to the total number of tiles. Since $f_L = a_{k-1} f_\alpha + a_k \sum_{i=0}^2 f_{\beta_i} + a_{k+1} f_\gamma$, we prove that each L tile belongs to $\alpha, \beta_i (i = 0, 1, 2)$ or γ domain, and β_3 domains never appear in the hexagonal metallic-mean tiling with $k \neq 1$. As for the golden-mean tiling with $k = 1$, α and β_0 domains do not appear, but β_3 domains appear due to the existence of the F vertices. The fractions of the β_1, β_2 , and γ

domains are given by Eqs. (21), (22), and (23), and the fraction of the β_3 domains is given as

$$f_{\beta_3} = \frac{r_1 f_F}{\tau_1^2} = \frac{5 + 3\tau_1}{31\tau_1^9}. \quad (24)$$

We show in Supplementary Fig. 5 the fraction of the L tiles which belong to each domain. When k is small, the



Supplementary Fig. 5. **a** Fractions of α, β_i ($i = 0, 1, 2, 3$), and γ domains for the total number of the domains are shown as the cumulative bar chart. **b** Fraction of the L tiles belonging to each domain are shown as the cumulative bar chart.

β_1 , β_2 , and γ domains are majority in the tilings. On the other hand, when the system approaches the honeycomb lattice, α and β_0 domains become dominant in the system. This originates from the fact that, in the large k case, the vertices are almost composed of the C_1 and C_0 vertices, and thereby α and β_0 domains, which are generated by applying the deflation operation to the above vertices, become dominant.

Supplementary Note 4 Domain boundaries

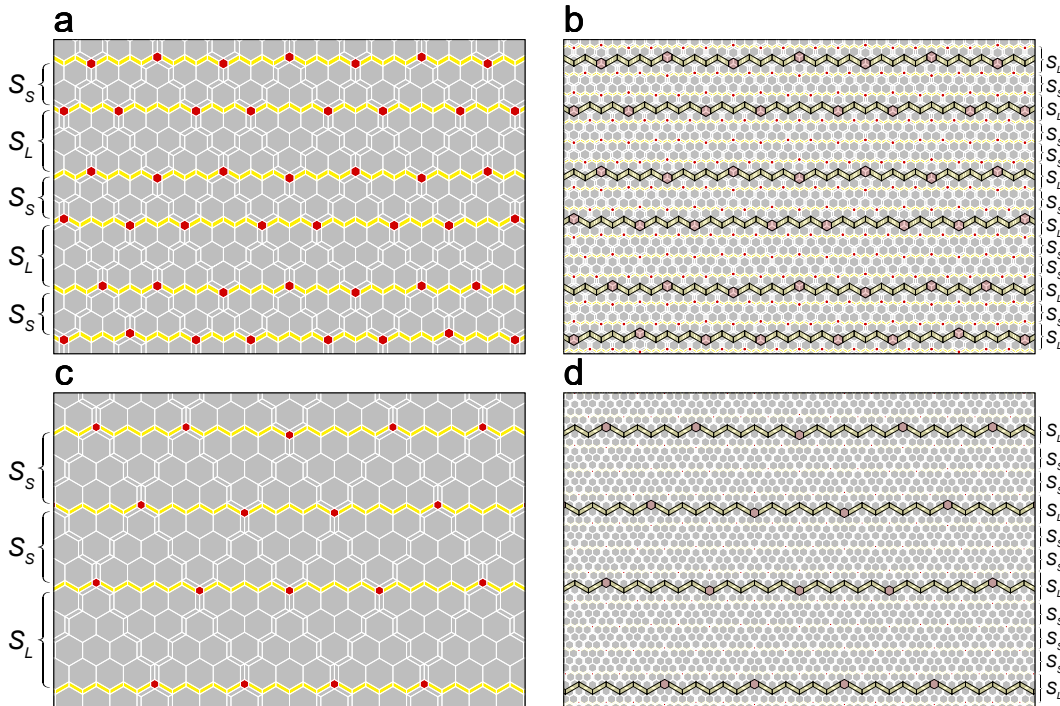
Honeycomb domains are separated by the P and S tiles and are distributed like triangular structure, as shown in Supplementary Fig. 2. This may allow us to regard the hexagonal metallic-mean tilings as the honeycomb lattice modulated by the one-dimensional domain boundaries along three directions with the angles $\theta = 0$ and $\pm\pi/3$. Here, we clarify how the domain boundaries are distributed in the metallic-mean tilings with $k \neq 1$.

Supplementary Figures 6a and 6c show the domain boundaries along the horizontal direction as colored tiles for $k = 2$ and $k = 3$. Each domain boundary is composed of the P and S tiles, and adjacent P tiles always share their shorter edges. We find that each P tile is adjacent to its reflected P tile (\bar{P} tile) or an S tile. Therefore, the zigzag chains of P tiles appear in the domain boundary. We note that three domain boundaries with distinct directions do not share any P tiles, but always cross at a certain S tile.

Now, we discuss how the domain boundaries along a certain direction are arranged in the metallic-mean tilings. We find in Supplementary Figs. 6a and 6c that the spaces between the domain boundaries are classified by two groups \mathcal{S}_S and \mathcal{S}_L . In the smaller space \mathcal{S}_S , there exist the α and β honeycomb domains, and in the other space \mathcal{S}_L , β and γ domains appear. To clarify the distributions of these spaces, we use the substitution rule of the tiles. Supplementary Figures 6b and 6d show the deflations of the tilings shown in Supplementary Figs. 6a and 6c, respectively. When the deflation operation is applied to the tiling, k and $k + 1$ domain boundaries are equally-spaced generated in the original \mathcal{S}_S and \mathcal{S}_L spaces, respectively. Namely, $k - 1$ and k \mathcal{S}_S are generated. On the other hand, under one deflation operation, one \mathcal{S}_L is generated at each domain boundary. Therefore, the numbers of \mathcal{S}_S and \mathcal{S}_L at iteration n ($N_{\mathcal{S}_S}$ and $N_{\mathcal{S}_L}$) satisfy

$$\begin{pmatrix} N_{\mathcal{S}_S}^{(n+1)} \\ N_{\mathcal{S}_L}^{(n+1)} \end{pmatrix} = \begin{pmatrix} k-1 & k \\ 1 & 1 \end{pmatrix} \begin{pmatrix} N_{\mathcal{S}_S}^{(n)} \\ N_{\mathcal{S}_L}^{(n)} \end{pmatrix}, \quad (25)$$

where the maximum eigenvalue is given by τ_k and the corresponding eigenvector $(k\tau_k, 1 + \tau_k)^T$. This means that the self-similarity inherent in the metallic ratio τ_k appears in the tiles, honeycomb domains, and spaces between adjacent domain boundaries.



Supplementary Fig. 6. **a** (**c**) The colored tiles represent the domain boundaries along the horizontal direction for the hexagonal silver-mean (bronze-mean) tiling with $k = 2$ ($k = 3$). **b** (**d**) The tilings are obtained by applying the deflation operation to the ones shown in **a** (**c**). The transparent tiles represent the original domain boundaries along the horizontal direction.

Supplementary Note 5 Higher-dimensional representation

Perpendicular space

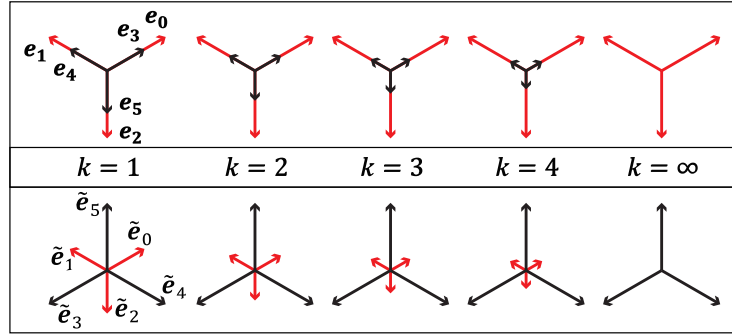
In this section, we consider the perpendicular space, introducing the six-dimensional representations of the vertices. First, we describe the vertex site in the two-dimensional physical space \mathcal{S} by six vectors \mathbf{e}_m and six integer indices $\vec{n} = (n_0, n_1, n_2, n_3, n_4, n_5)^T$, as

$$\mathbf{r} = (x, y) = \sum_{m=0}^5 n_m \mathbf{e}_m, \quad (26)$$

with

$$\mathbf{e}_m = \begin{cases} \left(\ell \cos(m\phi + \theta), \ell \sin(m\phi + \theta) \right) & m = 0, 1, 2 \\ \left(s \cos(m\phi + \theta), s \sin(m\phi + \theta) \right) & m = 3, 4, 5 \end{cases}, \quad (27)$$

where $\phi = 2\pi/3$ and θ is constant. ℓ and s are the lengths for longer and shorter edges of the tiles. The vectors \mathbf{e}_m are schematically shown in Supplementary Fig. 7.



Supplementary Fig. 7. Real space basis $\mathbf{e}_0, \dots, \mathbf{e}_5$ and perpendicular space basis $\tilde{\mathbf{e}}_0, \dots, \tilde{\mathbf{e}}_5$.

In Eq. (26), the vertex site \mathbf{r} can be regarded as the projection from a six-dimensional lattice point, where the vectors \mathbf{e}_m are the projections from the six-dimensional basis vectors. Thereby one can define the projections onto the other four-dimensional space (perpendicular space). For a unified understanding of the projection, it is convenient to introduce the six-dimensional space \mathcal{S}^h including the physical and perpendicular spaces. Then, \vec{n} is mapped to the six-dimensional lattice point \vec{r}^h in \mathcal{S}^h as,

$$\vec{r}^h = M\vec{n}, \quad (28)$$

$$M = \begin{pmatrix} \ell \cos \theta & \ell \cos(\phi + \theta) & \ell \cos(2\phi + \theta) & s \cos \theta & s \cos(\phi + \theta) & s \cos(2\phi + \theta) \\ \ell \sin \theta & \ell \sin(\phi + \theta) & \ell \sin(2\phi + \theta) & s \sin \theta & s \sin(\phi + \theta) & s \sin(2\phi + \theta) \\ \tau_k^{-1} \cos \theta & \tau_k^{-1} \cos(\phi + \theta) & \tau_k^{-1} \cos(2\phi + \theta) & -\cos \theta & -\cos(\phi + \theta) & -\cos(2\phi + \theta) \\ \tau_k^{-1} \sin \theta & \tau_k^{-1} \sin(\phi + \theta) & \tau_k^{-1} \sin(2\phi + \theta) & -\sin \theta & -\sin(\phi + \theta) & -\sin(2\phi + \theta) \\ \sqrt{2}\tau_k^{-1} & \sqrt{2}\tau_k^{-1} & \sqrt{2}\tau_k^{-1} & 0 & 0 & 0 \\ 0 & 0 & 0 & -\sqrt{2} & -\sqrt{2} & -\sqrt{2} \end{pmatrix}, \quad (29)$$

where M is the mapping matrix. Then, one can discuss vertex properties in both physical and perpendicular space. Namely, in the physical space \mathcal{S} , the vertex site \mathbf{r} is given by the first two components of the vector as

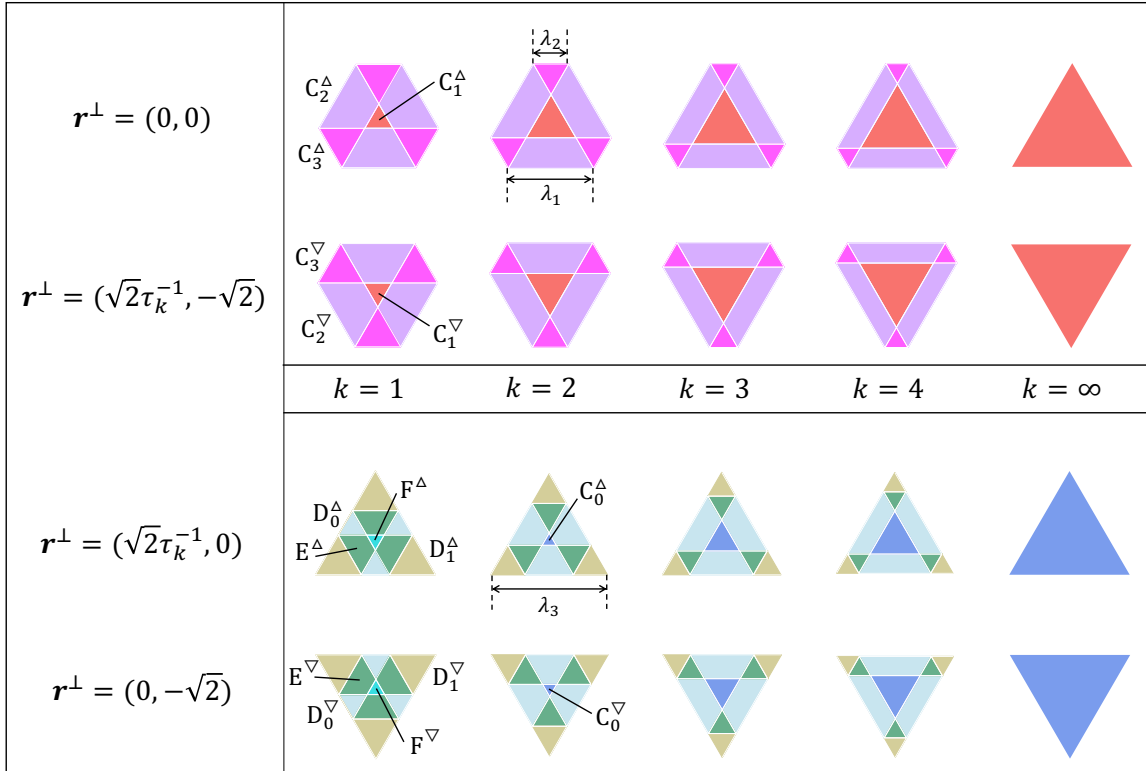
$$\mathbf{r} = \left((\vec{r}^h)_0, (\vec{r}^h)_1 \right) = \sum_{m=0}^5 n_m \mathbf{e}_m. \quad (30)$$

The four-dimensional perpendicular space is split into two-dimensional spaces $\tilde{\mathcal{S}}$ and \mathcal{S}^\perp , and the corresponding coordinates $\tilde{\mathbf{r}}$ and \mathbf{r}^\perp are given as

$$\tilde{\mathbf{r}} = \left((\tilde{r}^h)_2, (\tilde{r}^h)_3 \right) = \sum_{m=0}^5 n_m \tilde{\mathbf{e}}_m, \quad (31)$$

$$\mathbf{r}^\perp = \left((\tilde{r}^h)_4, (\tilde{r}^h)_5 \right) = \sum_{m=0}^5 n_m \mathbf{e}_m^\perp, \quad (32)$$

where $\tilde{\mathbf{e}}_m = (M_{2m}, M_{3m})$ and $\mathbf{e}_m^\perp = (M_{4m}, M_{5m})$. We find that $\mathbf{r}^\perp = (x^\perp, y^\perp)$ takes four values $x^\perp = 0, \sqrt{2}\tau_k^{-1}$ and $y^\perp = -\sqrt{2}, 0$ in the hexagonal metallic-mean tilings. In each \mathbf{r}^\perp plane, the $\tilde{\mathbf{r}}$ points densely cover a certain window. We find that the window in planes $\mathbf{r}^\perp = (0, 0), (\sqrt{2}\tau_k^{-1}, -\sqrt{2}) [(0, -\sqrt{2}), (\sqrt{2}\tau_k^{-1}, 0)]$ has a hexagonal (triangular) structure. Supplementary Figure 8 shows the perpendicular spaces for the hexagonal metallic-mean tilings with

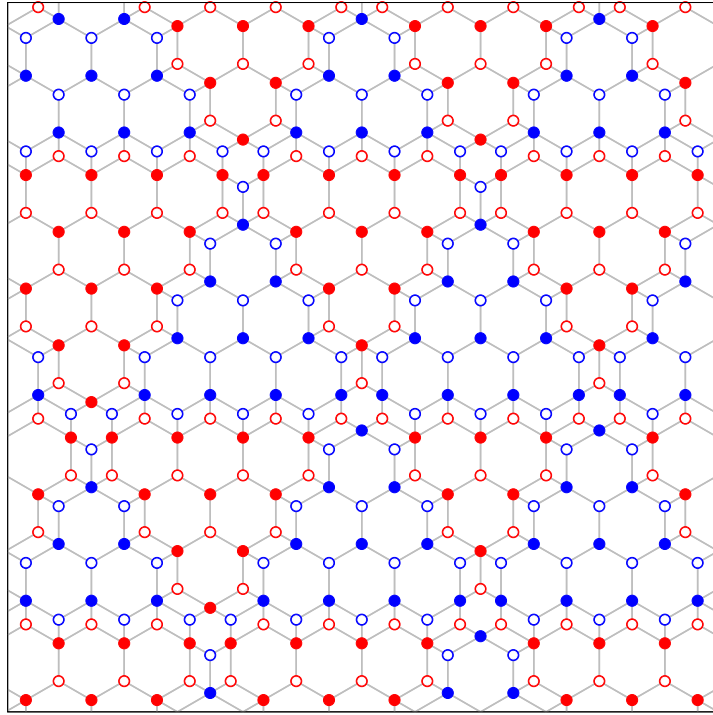


Supplementary Fig. 8. Perpendicular spaces $[\mathbf{r}^\perp = (0, 0), (\sqrt{2}\tau_k^{-1}, -\sqrt{2}), (\sqrt{2}\tau_k^{-1}, 0), \text{ and } (0, -\sqrt{2})]$ of the hexagonal metallic-mean tilings for $k = 1, 2, 3, 4,$ and ∞ . Each area bounded by the solid lines is the region of one of eight types of vertices with \triangle and ∇ . λ_1 and λ_2 (λ_3) are the characteristic lengths of the windows with $\mathbf{r}^\perp = (0, 0)$ and $(\sqrt{2}\tau_k^{-1}, -\sqrt{2})$ $[(\sqrt{2}\tau_k^{-1}, 0)$ and $(0, -\sqrt{2})]$.

$k = 1, 2, 3, 4,$ and ∞ . The characteristic lengths λ_1, λ_2 and λ_3 will be obtained in Supplementary Note 6. We find that eight types of vertices are mapped into specific regions. This implies that the perpendicular spaces reflect the local environments for the lattice sites. Namely, the areas of each vertex region in perpendicular spaces are proportional to its fraction in the physical space. The region of the F (C_0) vertices appears only in the case of $k = 1$ ($k \neq 1$). This means the absence of C_0 (F) vertices in the hexagonal metallic-mean tilings with $k = 1$ ($k \neq 1$), which is consistent with the results discussed in the main text and Supplementary Note 2. The areas of the C_0, C_1 vertices (the others) monotonically increase (decrease) with increasing k . The planes $\mathbf{r}^\perp = (0, 0)$ and $(\sqrt{2}\tau_k^{-1}, -\sqrt{2}) [(0, -\sqrt{2})$ and $(\sqrt{2}\tau_k^{-1}, 0)]$ are fully occupied only by the C_0 and C_1 vertices in the limit $k \rightarrow \infty$ since $f_{C_0}, f_{C_1} \rightarrow 1/2$. We also find that the vertices in the A (B) sublattice are mapped to the planes with $(0, 0)$ and $(\sqrt{2}\tau_k^{-1}, -\sqrt{2}) [(0, -\sqrt{2})$ and $(\sqrt{2}\tau_k^{-1}, 0)]$. This can be explained by the following. The sublattice index for each vertex is uniquely determined, as discussed above. Since upon moving from one site to its neighbor only one of the n_m 's changes by ± 1 , the site

with an even (odd) number $(\tau_k x^\perp + y^\perp)/\sqrt{2}$ corresponds to the A (B) sublattice. Correspondingly, the areas for both sublattices are different from each other, meaning the existence of the sublattice imbalance in the system.

We wish to note that the perpendicular space analysis clarifies whether each vertex belongs to the honeycomb domain with \triangle or ∇ . As seen in Supplementary Fig. 9, the vertices in the space $\mathbf{r}^\perp = (\sqrt{2}\tau_k^{-1}, -\sqrt{2})$ and $(0, -\sqrt{2})$ [(0,0) and $(\sqrt{2}\tau_k^{-1}, 0)$] belong to the honeycomb domain with \triangle (∇). This can be explained by the following. Each honeycomb domain is composed of only L tiles. When one moves within the domain, the longer length appears in the physical space, changing x^\perp . Therefore, we find that vertices in a certain honeycomb domain take the common value of y^\perp . Furthermore, any honeycomb domains with α ($= \triangle$ or ∇) are adjacent to the honeycomb domains with $\bar{\alpha}$ across the single boundary composed of the zig-zag P tiles, as discussed in the main text. When one moves from one honeycomb domain to its neighboring honeycomb domain, one shorter length appears in the physical space, changing y^\perp by $\pm\sqrt{2}$. Therefore, we find that vertices of the adjacent domains take the different values of y^\perp each other, and understand that vertices, which are mapped to the perpendicular spaces $\mathbf{r}^\perp = (\sqrt{2}\tau_k^{-1}, -\sqrt{2})$ and $(0, -\sqrt{2})$ [(0,0) and $(\sqrt{2}\tau_k^{-1}, 0)$], belong to the honeycomb domains with \triangle (∇). By these reasons, the perpendicular analysis clarifies not only the sublattice structure but also the honeycomb domain structure. One can define the vertex belonging to the honeycomb domain with α ($= \triangle, \nabla$) as X^α , where X ($= C_0, C_1, \dots, F$). Namely, the fractions for X^\triangle and X^∇ are identical since the corresponding areas are identical in the perpendicular space.

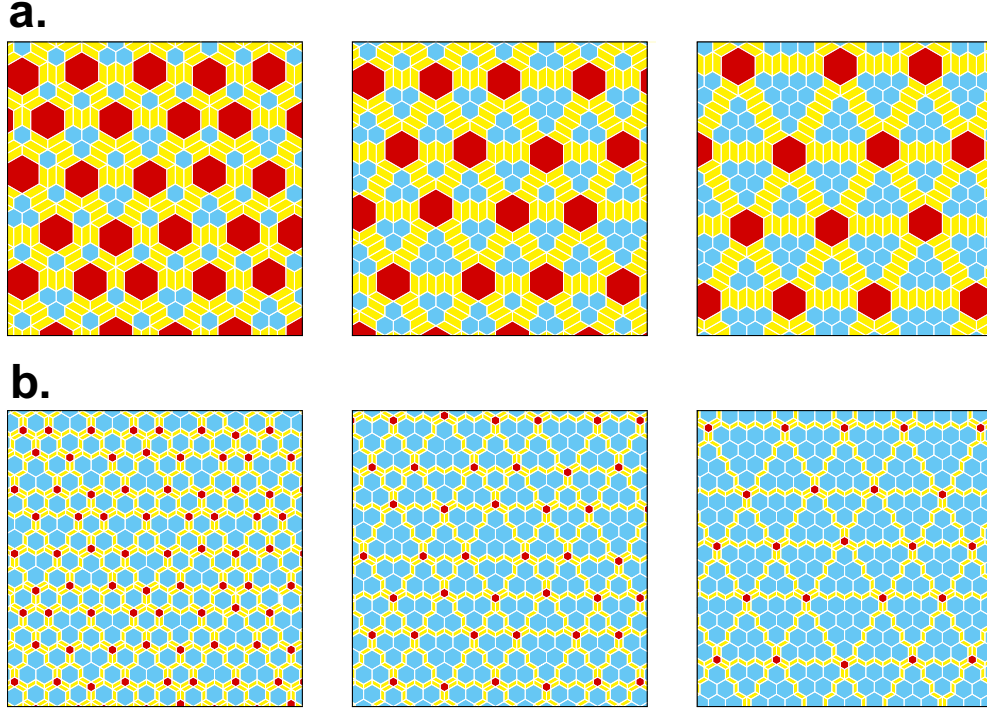


Supplementary Fig. 9. Hexagonal bronze-mean tiling with vertices classified according to their coordinates in the perpendicular space \mathbf{r}^\perp . Red open, blue open, red filled, and blue filled circles represent the vertices, which are mapped to the perpendicular space with $\mathbf{r}^\perp = (0, 0), (\sqrt{2}\tau_k^{-1}, -\sqrt{2}), (\sqrt{2}\tau_k^{-1}, 0)$ and $(0, -\sqrt{2})$, respectively. The blue (red) symbols belong to honeycomb domains with \triangle (∇).

Cut-and-project scheme

In the six-dimensional representations, we have introduced two lengths ℓ and s , and the metallic mean τ_k . Note that, in Eq. (29), the length scale appears only in the physical space and the metallic mean appears only in the perpendicular space. This may mean that the metallic mean is important in the perpendicular space while plays no role in the physical space. This allows us to generate the hexagonal metallic-mean tilings with arbitrary lengths ℓ and s , in contrast to the tilings generated by means of the substitution rule. This is known as the cut-and-project scheme, which should be useful to clarify how relevant the tiling is for the atomic position in the MC and MD simulations discussed in the main text.

The six-dimensional lattice points \vec{r}^h with indices \vec{n} relevant for the generalized hexagonal metallic-mean tiling satisfies the condition that their projections onto the perpendicular space are located inside the windows, which are shown in Supplementary Fig. 8. Then, projecting these six-dimensional coordinates onto the physical space, we can obtain the generalized hexagonal tilings. Golden-mean, silver-mean, and bronze-mean tilings with $\ell/s = 1/2$ and $\ell/s = 2$ generated by means of the cut-and-project scheme are shown in Supplementary Fig. 10. We wish to note that the self-similarity in the tilings is inherent in the case $\ell/s = \tau_k$ and the substitution rule cannot be defined in generic case with arbitrary ℓ and s .



Supplementary Fig. 10. Hexagonal golden-, silver- and bronze-mean tilings generated by the cut-and-project scheme with **a** $\ell/s = 1/2$ and **b** $\ell/s = 2$.

Reciprocal vectors

Each vertex site in the tilings is described by the six integer indices \vec{n} and that mapped to the six-dimensional space \mathcal{S}^h is represented as

$$\vec{r}^h = M\vec{n} = \sum_i n_i \vec{e}_i^h, \quad (33)$$

where \vec{e}_i^h ($i = 0, 1, \dots, 5$) are the six kinds of six-dimensional basis vectors with $(\vec{e}_i^h)_j [= M_{ij}]$. The six kinds of six-dimensional reciprocal vectors \vec{q}_i^h are obtained by imposing the condition $\vec{e}_i^h \cdot \vec{q}_j^h = 2\pi\delta_{ij}$ with δ_{ij} is Kronecker

delta. These are explicitly given as,

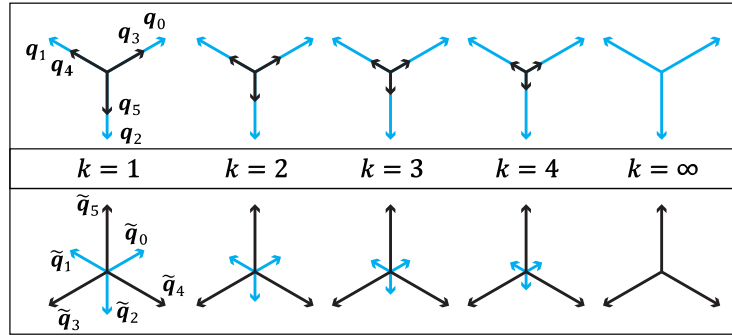
$$\vec{q}_m^h = C \begin{pmatrix} \cos(m\phi + \theta) \\ \sin(m\phi + \theta) \\ s \cos(m\phi + \theta) \\ s \sin(m\phi + \theta) \\ (\ell\tau_k + s)/(2\sqrt{2}) \\ 0 \end{pmatrix} \quad \text{for } m = 0, 1, 2, \quad (34)$$

$$\vec{q}_m^h = C \begin{pmatrix} \tau_k^{-1} \cos(m\phi + \theta) \\ \tau_k^{-1} \sin(m\phi + \theta) \\ -\ell \cos(m\phi + \theta) \\ -\ell \sin(m\phi + \theta) \\ 0 \\ -(\ell + s\tau_k^{-1})/(2\sqrt{2}) \end{pmatrix} \quad \text{for } m = 3, 4, 5, \quad (35)$$

where $C = 4\pi/[3(\ell + s\tau_k^{-1})]$. The reciprocal vectors projected onto the physical space are given as,

$$\mathbf{q}_m = \left((\vec{q}_m^h)_0, (\vec{q}_m^h)_1 \right). \quad (36)$$

The six reciprocal vectors are composed of three long vectors $\mathbf{q}_0, \mathbf{q}_1, \mathbf{q}_2$ and three short vectors $\mathbf{q}_3, \mathbf{q}_4, \mathbf{q}_5$. The ratio of their lengths is given by τ_k . The longer length $|\mathbf{q}_0| = |\mathbf{q}_1| = |\mathbf{q}_2| = 4\pi/[3(\ell + s\tau_k^{-1})]$ monotonically increases with increasing k and approaches the constant $4\pi/(3\ell)$ in larger k . On the other hand, the shorter length $|\mathbf{q}_3| = |\mathbf{q}_4| = |\mathbf{q}_5| = 4\pi/[3(\ell\tau_k + s)]$ monotonically decreases and vanishes in the limit $k \rightarrow \infty$. This is consistent with the fact that, in the limit $k \rightarrow \infty$, three of the reciprocal vectors are reduced to those for the honeycomb lattice and the metallic-mean tiling can be regarded as the aperiodic approximant of the honeycomb lattice. We wish to note that the net number of the reciprocal vectors is two due to satisfying $\mathbf{q}_0 = -(\mathbf{q}_1 + \mathbf{q}_2)$ in the limit $k \rightarrow \infty$. This is consistent with the fact that the honeycomb lattice is periodic.



Supplementary Fig. 11. Reciprocal lattice basis in the real space $\mathbf{q}_0, \dots, \mathbf{q}_5$ and those in the perpendicular space $\tilde{\mathbf{q}}_0, \dots, \tilde{\mathbf{q}}_5$.

Supplementary Note 6 Phason flips

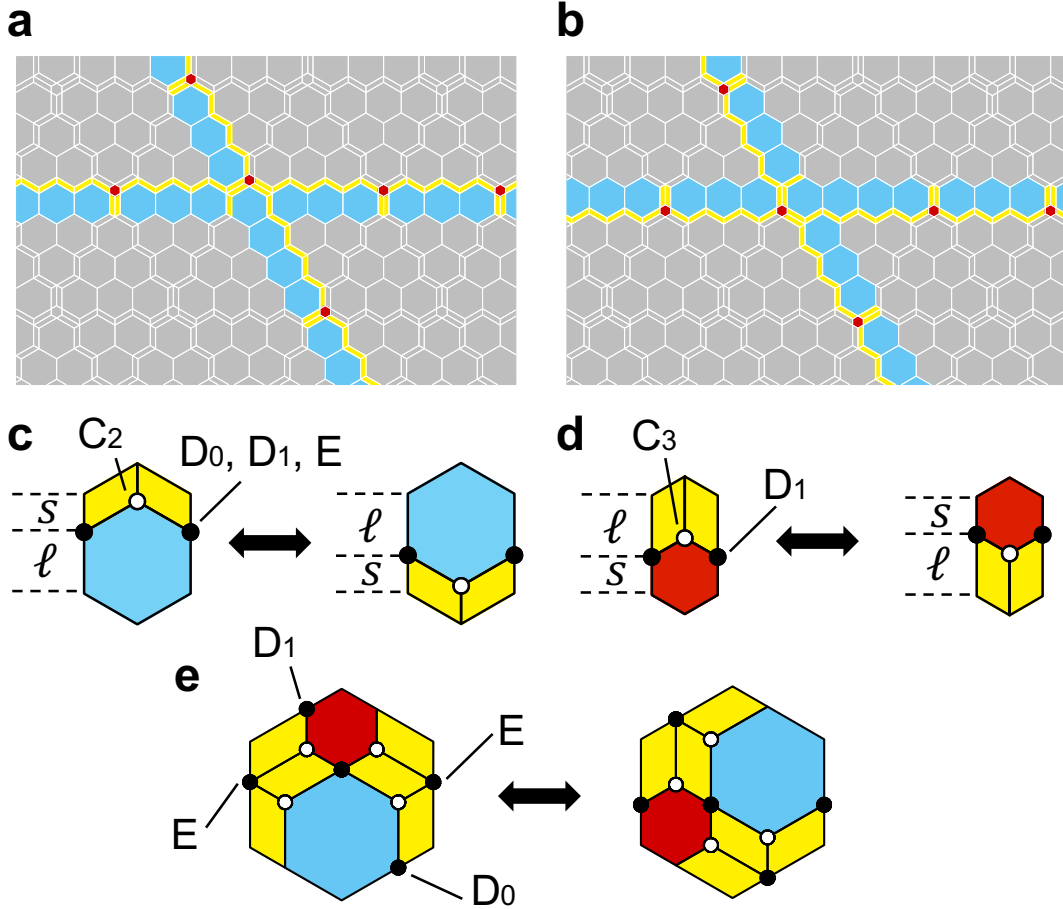
We examine phason flips in the hexagonal metallic-mean tilings. As seen in Supplementary Note 5, the vertices in the metallic-mean tilings can be mapped inside of the windows in the perpendicular space. When the windows in the perpendicular space slightly slide, positions for some vertices become located outside of the windows and those for some vertices become located inside. This slightly changes the vertex structure in the physical space, that is, some vertices can be regarded to move, so called, phason flips. To discuss how the phason flips occur in the metallic-mean tiling, we show the bronze-mean tiling and the tiling with the slightly shifted windows in Supplementary Figs. 12a and 12b. For clarify, the difference between these two tilings is shown in color. We find the phason flip along a certain domain boundary. Furthermore, we find that this change can be described by three kinds of local flips. Note that a single local flip never appears due to the matching rule of the tilings. One of local flips is the position change around the C_2 vertex sharing one L tile and two P tiles, as shown in Supplementary Fig. 12c, where the C_2 vertex and the D_0 , D_1 and E vertices connected to it by the longer edges change their positions. The local flip around the C_3 vertex also occurs at the same time, as shown in Supplementary Fig. 12d, where the C_3 vertex and the D_1 vertices connected to it by the shorter edges change their positions. The other flip appears at the intersection of two domain boundaries, as shown in Supplementary Fig. 12e. In the case, some D_0 , D_1 and E vertices change their positions. When one focuses on the E vertex, the change in the physical space is characterized by $\mathbf{e}_2 - \mathbf{e}_0$, as shown in Supplementary Fig. 13a. The corresponding move in the perpendicular space appears between the corners of the triangular window for E vertices, which is characterized by $\tilde{\mathbf{e}}_2 - \tilde{\mathbf{e}}_0$ schematically shown in Supplementary Fig. 13b. Therefore, an edge length of the window of E vertex in the perpendicular space (if $k = 1$, a longer edge length of the trapezoid) is $|\tilde{\mathbf{e}}_2 - \tilde{\mathbf{e}}_0| = \sqrt{3}\tau_k^{-1}$. We immediately obtain the characteristic lengths of the windows in the perpendicular space as,

$$\lambda_1 = \sqrt{3}, \quad (37)$$

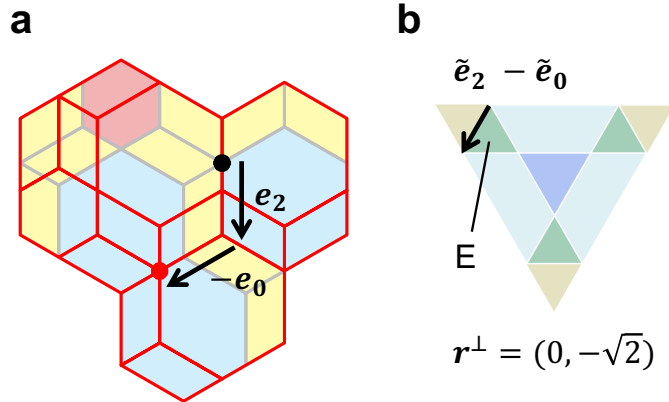
$$\lambda_2 = \sqrt{3}\tau_k^{-1}, \quad (38)$$

$$\lambda_3 = \sqrt{3}(1 + \tau_k^{-1}). \quad (39)$$

We note that the above phason flip also changes the areas of the honeycomb domains. This should be observed as thermal fluctuations of Monte Carlo and MD simulations² (See the main text for the details).



Supplementary Fig. 12. Schematic pictures for the phason flips in the hexagonal bronze-mean tiling. **a** and **b** show the bronze-mean tiling and the tiling with the slightly shifted windows, respectively. The difference is explicitly shown in color. **c** (**d**) The local flips around the C_2 (C_3) vertex, **e** The local flip at the intersection of two domain boundaries. In **c,d** and **e**, circles represent the vertices which move due to the phason flip.



Supplementary Fig. 13. **a** The position change of the E vertex due to the phason flip. The black (red) circle indicates the position of the E vertex before (after) the flip. **b** shows the corresponding position change in the perpendicular space $r^\perp = (0, -\sqrt{2})$.

Supplementary Note 7 Lattice structure factors

We study the lattice structure factors of the hexagonal metallic-mean tilings in detail. Supplementary Figure 14a shows the lattice structure factors for each k , where the circular area corresponds to the weight of the peak. It is clearly found that the structure factor have the sixfold rotational symmetry, meaning that the metallic-mean tilings have a hexagonal symmetry.

To clarify how the peak structure is changed with varying k , we show in Supplementary Fig. 14b (c) the crosssection of the lattice structure factors on two mirror axes, which are explicitly shown as the yellow (red) line in Supplementary Fig. 14a. When $k \rightarrow \infty$, the peaks are periodically distributed since the system is reduced to the honeycomb lattice. These positions are spanned by $\mathbf{q}_0, \mathbf{q}_1$ and \mathbf{q}_2 , and the weights of the peaks take two values, 1 and 0.25, as shown in Supplementary Figs. 14b and 14c. Decreasing k , main peaks remain with larger weights and satellite peaks with smaller weights are induced slightly away from the main peaks. The main peak positions are mainly spanned by $\mathbf{q}_0, \mathbf{q}_1$ and \mathbf{q}_2 . On the other hand, the other peak positions are represented by six reciprocal vectors as

$$\mathbf{Q} = \sum_{m=0}^5 \tilde{n}_m \mathbf{q}_m, \quad (40)$$

where \tilde{n}_m is an integer. These are consistent with the fact that the metallic-mean tilings are quasiperiodic. Furthermore, the existence of the satellite peaks originates from the incommensurate modulated structure formed by the domain boundary composed of P tiles in the real space. When $k \leq 4$, the main peaks with large weights are represented by six reciprocal vectors, which are shown as the blue circles in Supplementary Figs. 14b and 14c. This means that the vertex structures for small k are no longer described by the modulated honeycomb lattice.

Here, we calculate the lattice structure factors. The density of the vertex sites in the tiling is given by $\rho(\mathbf{r}) = \sum_j \delta(\mathbf{r}_j - \mathbf{r})$, where δ is the delta function and \mathbf{r}_i represents the position of the i th vertex site. The summation is over all vertex sites in the tiling. The lattice structure factors are give by $|\rho(\mathbf{q})|^2$, where

$$\rho(\mathbf{q}) = \int \rho(\mathbf{r}) \exp(-i\mathbf{r} \cdot \mathbf{q}) d\mathbf{r} = \sum_j \exp(-i\mathbf{r}_j \cdot \mathbf{q}). \quad (41)$$

It is convenient to make use of the higher-dimensional representation discussed in Supplementary Note 5. Since the six-dimensional basis and reciprocal vectors \vec{e}_m^h and \vec{q}_m^h satisfy the orthogonal relation $\vec{e}_m^h \cdot \vec{q}_n^h = 2\pi\delta_{mn}$, we obtain

$$\exp(i\vec{e}_m^h \cdot \vec{q}_n^h) = \exp(i\mathbf{e}_m \cdot \mathbf{q}_n) \exp(i\tilde{\mathbf{e}}_m \cdot \tilde{\mathbf{q}}_n) \exp(i\mathbf{e}_m^\perp \cdot \mathbf{q}_n^\perp) = 1, \quad (42)$$

where $\mathbf{r}_m(\mathbf{q}_m)$, $\tilde{\mathbf{r}}_m(\tilde{\mathbf{q}}_m)$, and $\mathbf{r}_m^\perp(\mathbf{q}_m^\perp)$ are the two-dimensional vectors in the spaces \mathcal{S} , $\tilde{\mathcal{S}}$, and \mathcal{S}^\perp , respectively. Therefore, we obtain

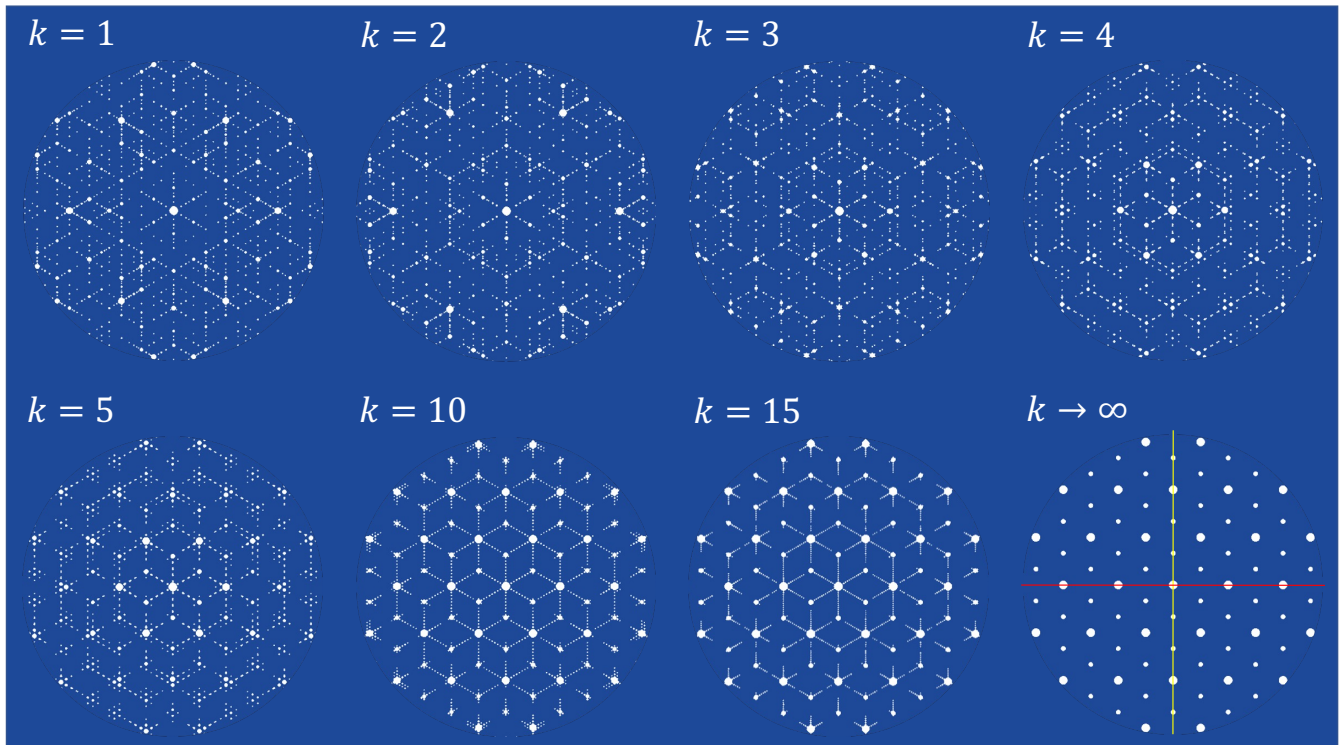
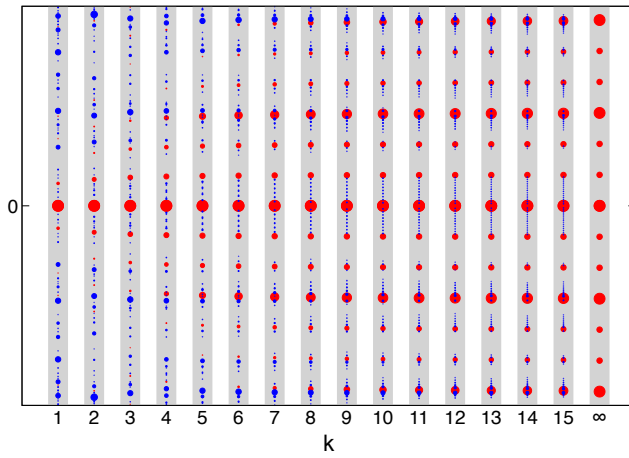
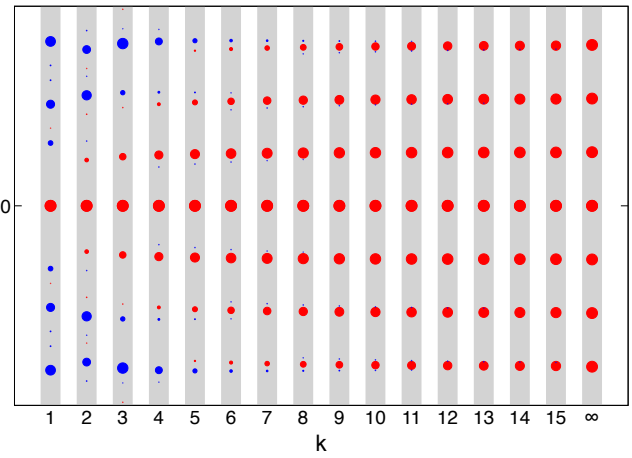
$$\rho(\mathbf{q}) = \sum_j \exp(i\tilde{\mathbf{r}}_j \cdot \tilde{\mathbf{q}}) \exp(i\mathbf{r}_j^\perp \cdot \mathbf{q}^\perp), \quad (43)$$

where the j th vertex site \mathbf{r}_j is mapped to $\tilde{\mathbf{r}}_j$ and \mathbf{r}_j^\perp in the perpendicular spaces $\tilde{\mathcal{S}}$ and \mathcal{S}^\perp . Each vertex site is mapped to the point in one of four domains with $\mathbf{r}^\perp = (0, 0), (\sqrt{2}\tau_k^{-1}, -\sqrt{2}), (\sqrt{2}\tau_k^{-1}, 0)$, and $(0, -\sqrt{2})$. Therefore, the equation (43) can be divided into four, as

$$\begin{aligned} \rho(\mathbf{q}) &= \mathcal{F}_{00}(\tilde{\mathbf{q}}) + \exp(i\sqrt{2}\tau_k^{-1}q_0^\perp)\mathcal{F}_{10}(\tilde{\mathbf{q}}) \\ &\quad + \exp(-i\sqrt{2}q_1^\perp)\mathcal{F}_{01}(\tilde{\mathbf{q}}) + \exp(i\sqrt{2}\tau_k^{-1}q_0^\perp)\exp(-i\sqrt{2}q_1^\perp)\mathcal{F}_{11}(\tilde{\mathbf{q}}), \end{aligned} \quad (44)$$

$$\mathcal{F}_{mn}(\tilde{\mathbf{q}}) = \sum_{j \in (mn)^\perp} \exp(i\tilde{\mathbf{r}}_j \cdot \tilde{\mathbf{q}}), \quad (45)$$

where \mathcal{F}_{mn} indicates the Fourier transform of the occupation domain in the perpendicular space with $(\tau_k x^\perp, -y^\perp)/\sqrt{2} = (m, n)$, which are explicitly shown as the hexagons and triangles shown in Supplementary Fig. 8. Then, we can evaluate the lattice structure factor $|\rho(\mathbf{q})|^2$.

a**b****c**

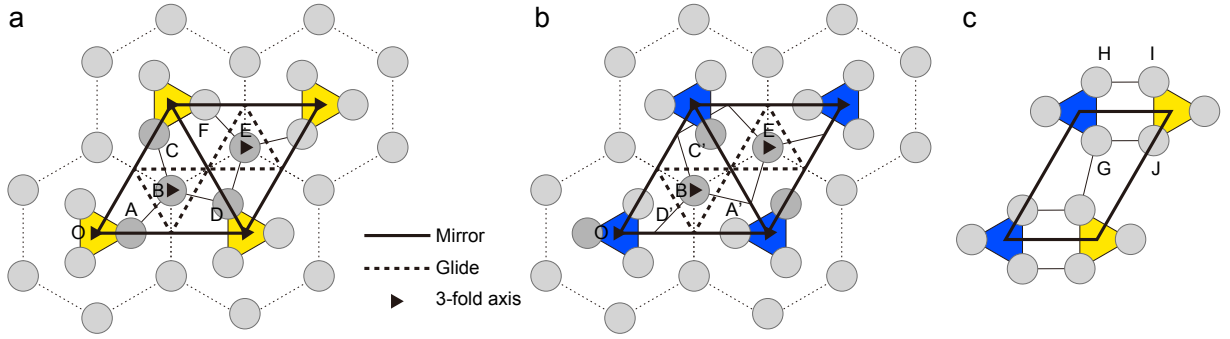
Supplementary Fig. 14. **a** The lattice structure factors for each k . **b** (**c**) The crosssection of the lattice structure factors on the mirror axis shown as the yellow (red) line in **a**. The red circles show peak positions spanned by only $\mathbf{q}_0, \mathbf{q}_1$ and \mathbf{q}_2 , and the blue circles show the others.

Supplementary Note 8 Crystallographic description of the P31m particle system

The particle system exhibits a regular structure with a plane group represented by P31m, as shown in Supplementary Fig. 15. A solid bold line indicates a mirror plane, and a dashed line indicates a glide plane. A solid triangle symbol indicates a three-fold rotation axis. This group is characterized by its 3-fold symmetry. Let A, B, C, D, E, and F be the centers of particles. As a result of this symmetry, we observe that the distances AB, BC, and BD are all equal. To further analyze the system, we make the assumption that there are two types of equilateral polygons present: pentagons and triangles. By considering the equality $AB = CF$, we can determine the positions of all the particles in the system. Within the unit cell, there are five particles, and their positions can be identified using the Wyckoff Positions 2b and 3c, as shown in the Supplementary Table 1. If the coordinates of particle A in Supplementary Fig. 15a is set to be $(c, 0)$, we find

$$c = \frac{\sqrt{33} - 3}{12} = 0.2287, \quad \overline{AB} = \overline{CF} = \sqrt{3}c = \frac{\sqrt{11} - \sqrt{3}}{4} = 0.3961. \quad (46)$$

It is important to note that while the pentagon (BCFED) in the particle system is equilateral, it is not a regular pentagon, for it is elongated along the mirror plane.



Supplementary Fig. 15. **a, b**, Plane group P31m for a particle system. **c**, Decoration of a parallelogram.

Wyckoff Position	Site Sym.	Points	Coordinates
2b	3..	B, E	$\left(\frac{1}{2}, \frac{\sqrt{3}}{6}\right), \left(1, \frac{\sqrt{3}}{3}\right)$
3c	..m	A, C, D	$(c, 0), \left(\frac{1}{2}(1-c), \frac{\sqrt{3}}{2}(1-c)\right), \left(1 - \frac{1}{2}c, \frac{\sqrt{3}}{2}c\right)$
3c	..m	A', C', D'	$(1-c, 0), \left(\frac{1+c}{2}, \frac{\sqrt{3}}{2}(1-c)\right), \left(\frac{1}{2}c, \frac{\sqrt{3}}{2}c\right)$

Supplementary Table 1. Wyckoff Position for a particle system. $c = \frac{\sqrt{33}-3}{12} = 0.2287$.

The basis vectors $\mathbf{a}_1, \mathbf{a}_2$ and the corresponding reciprocal basis vectors $\mathbf{b}_1, \mathbf{b}_2$ are given by

$$\mathbf{a}_1 = a(1, 0), \quad \mathbf{a}_2 = a\left(\frac{1}{2}, \frac{\sqrt{3}}{2}\right), \quad \mathbf{b}_1 = \frac{2\pi}{a}\left(1, -\frac{\sqrt{3}}{3}\right), \quad \mathbf{b}_2 = \frac{2\pi}{a}\left(0, \frac{2\sqrt{3}}{3}\right),$$

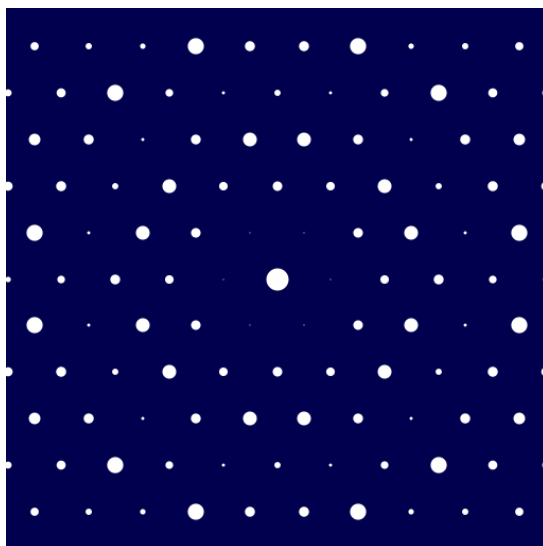
where a is the lattice constant (rhombus edge). For the reciprocal lattice vector $\mathbf{G} = h\mathbf{b}_1 + k\mathbf{b}_2$, the structure factor is evaluated as

$$F(h, k) = f \sum_{\alpha=A,B,C,D,E} \exp(2\pi i \mathbf{G} \cdot \mathbf{r}_\alpha). \quad (47)$$

The diffraction image calculated by this equation is shown in Supplementary Fig. 16.

Model for the metallic-mean tiling: Supplementary Figure 15c represents a decoration model for a parallelogram. If we assume that the rectangle GHIJ is a square; *i.e.* $\overline{AB} = \overline{CF} = \overline{GH} = \overline{GJ}$, then the length ratio of the tile is

$$\frac{s}{\ell} = (1 + \sqrt{3})c = 0.6249. \quad (48)$$



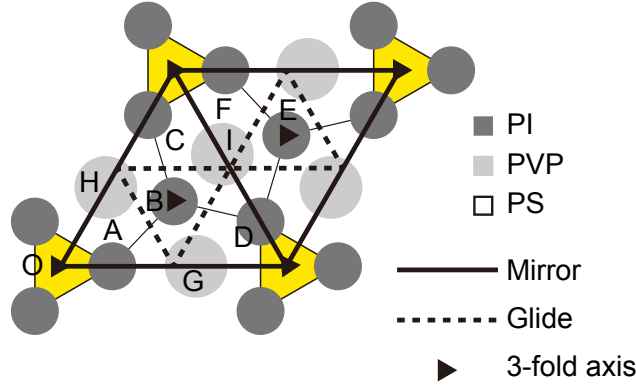
Supplementary Fig. 16. Diffraction image for P31m perfect crystal ($k \rightarrow \infty$) calculated by Eq. (48) rotated 90° . The area is proportional to the intensity.

Supplementary Note 9 Crystallographic description of the P31m polymer blend system

The same plane group is adopted by an ABC triblock terpolymer/homopolymer blend, where dark gray circles represent polyisoprene (PI), light gray circles represent poly(2-vinylpyridine) (PVP), and the matrix region is polystyrene (PS), as shown in Supplementary Fig. 17. We simply assume that domains of PI and PVP are all circles, and that the centers of polyisoprene domains occupy the same positions as the previous colloidal particle system. Let A, B, \dots , I be the centers of circular domains, and let the distance $\overline{OG} = d$ for the center positions of PVP. Although it is a crude treatment, we determine $d = \frac{3}{5}$ by minimizing the next (entropic) elastic free-energy function $S(d)$ inside a pentagon (BCFED):

$$S(d) \propto \overline{BI}^2 + \overline{CI}^2 + \overline{FI}^2 + \overline{EI}^2 + \overline{DI}^2 = \overline{AG}^2 + 2\overline{BG}^2 + 2\overline{DG}^2. \quad (49)$$

Wyckoff Positions for a polymer blend are shown in Supplementary Table 2.



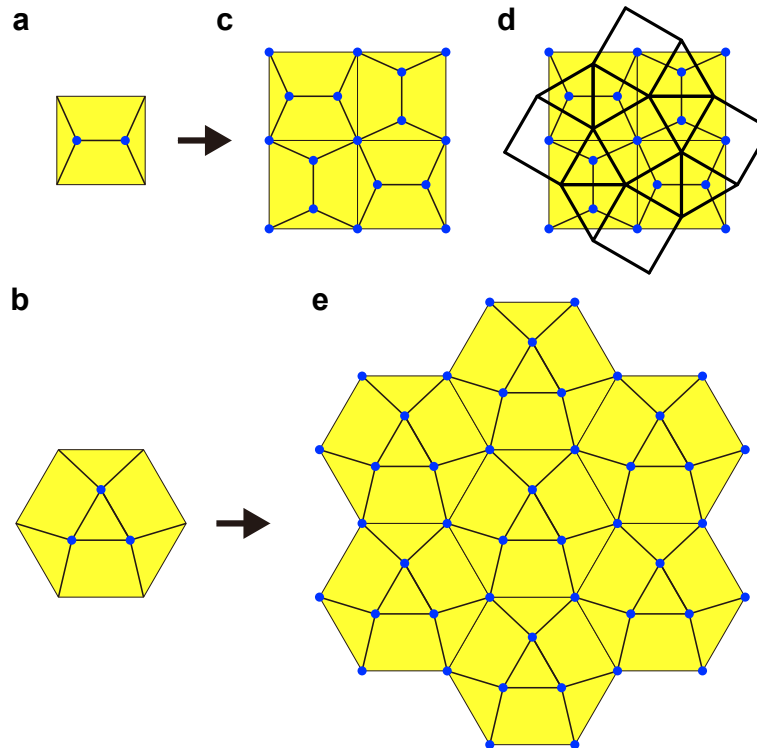
Supplementary Fig. 17. Plane group P31m for a polymer blend.

Polymer	Wyckoff Position	Site Sym.	Points	Coordinates
PI	2b	3..	B, E	$\left(\frac{1}{2}, \frac{\sqrt{3}}{6}\right), \left(1, \frac{\sqrt{3}}{3}\right)$
PI	3c	..m	A, C, D	$(c, 0), \left(\frac{1}{2}(1-c), \frac{\sqrt{3}}{2}(1-c)\right), \left(1 - \frac{1}{2}c, \frac{\sqrt{3}}{2}c\right)$
PVP	3c	..m	G, H, I	$(d, 0), \left(\frac{1}{2}(1-d), \frac{\sqrt{3}}{2}(1-d)\right), \left(1 - \frac{1}{2}d, \frac{\sqrt{3}}{2}d\right)$

Supplementary Table 2. Wyckoff Position for a polymer blend. $c = \frac{\sqrt{33}-3}{12} = 0.2287$ and $d = \frac{3}{5}$.

Supplementary Note 10 Pentagon tilings

We demonstrate the accommodation of pentagons within both a square and a hexagon. Firstly, we consider a square with two points placed inside (Supplementary Fig. 18a), and secondly, a hexagon with three points inside (Supplementary Fig. 18b). By connecting the points, we form pentagonal tilings. In Supplementary Fig. 18c, we present the equilateral Cairo pentagonal tiling, which serves as the dual of the $3^2.4.3.4$ Archimedean tiling with the $P4gm$ plane group (Supplementary Fig. 18d). The $3^2.4.3.4$ Archimedean tiling is associated with the σ phase found in complex metallic and soft-matter phases. It is recognized as a periodic approximant of dodecagonal quasicrystals. Additionally, Supplementary Figure 18e illustrates a 3-fold equilateral pentagon-triangle tiling with the $P31m$ plane group discussed in the present paper. Despite their distinct symmetries, these two structures are closely related and are commonly observed in soft-matter systems.



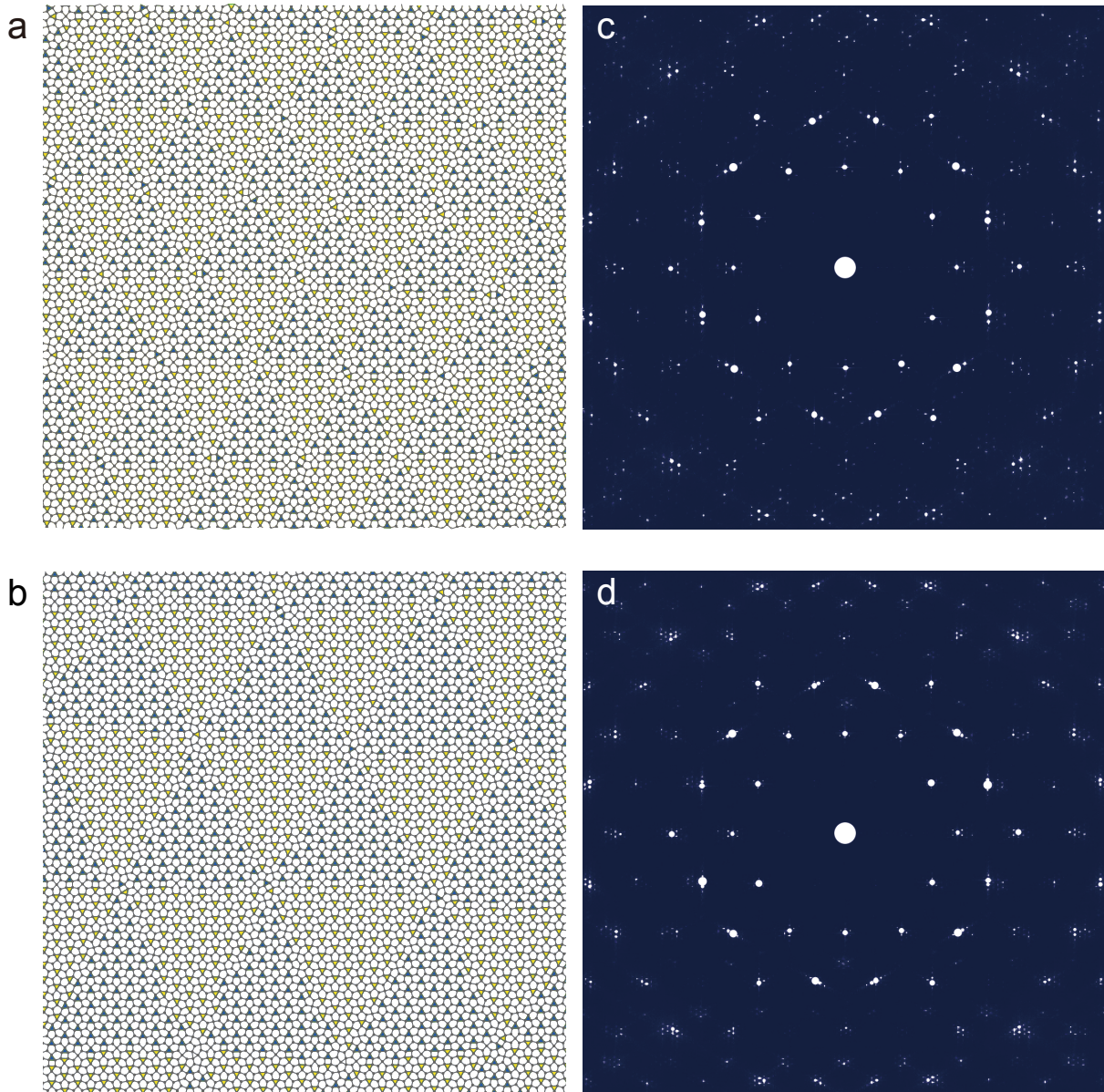
Supplementary Fig. 18. Equilateral pentagon tilings. **a**, elemental square, **b** elemental hexagon, **c**, 4-fold pentagonal Cairo tiling, **d**, duality of the Cairo tiling and the $3^2.4.3.4$ Archimedean tiling, **e**, 3-fold pentagon-triangle tiling.

Supplementary Note 11 Colloidal system

Engle used the Lennard-Jones-Gauss potential of the form^{2,3}:

$$V(r) = \frac{1}{r^{12}} - \frac{2}{r^6} - \epsilon \exp\left(-\frac{(r - r_0)^2}{2\sigma^2}\right), \quad (50)$$

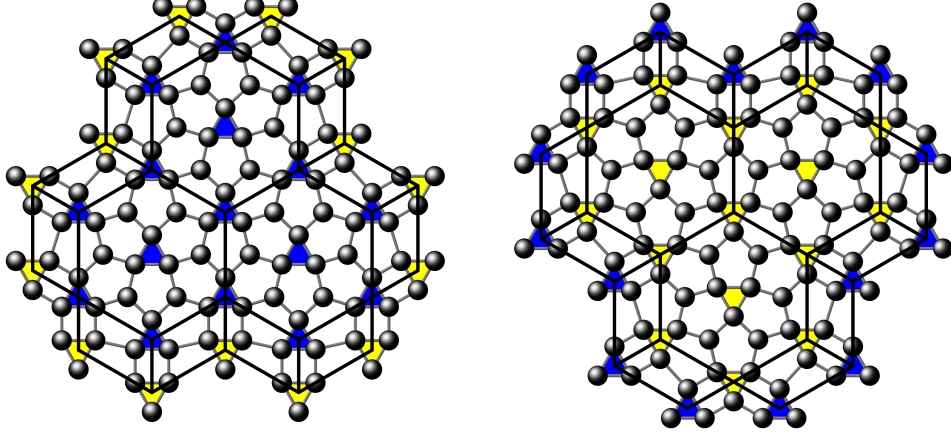
with parameters $\sigma^2 = 0.042$, $\epsilon = 1.8$, $r_0 = 1.42$. We have conducted Monte Carlo simulation with NPT ensemble at $T = 0.29$ and $T = 0.28$, $P = 0.0$, and $N = 19740$. Snapshots of modulated structures quenched at $T = 0.12$ are displayed in Supplementary Fig. 19 (**a**, $T = 0.29$ and **b**, $T = 0.28$). The diffraction images in Supplementary Fig. 19 (**c**, $T = 0.29$ and **d**, $T = 0.28$) are obtained by the average of 200 Fourier transforms of quenched samples at $T = 0.12$. In contrast to the diffraction image for the P31m perfect crystal, satellite peaks are observed.



Supplementary Fig. 19. Colloidal simulation. Modulated domain structure (**a**, $T = 0.29$ and **b**, $T = 0.28$) and Diffraction image (**c**, $T = 0.29$ and **d**, $T = 0.28$). The area is proportional to the intensity.

Supplementary Note 12 Atomic decorations

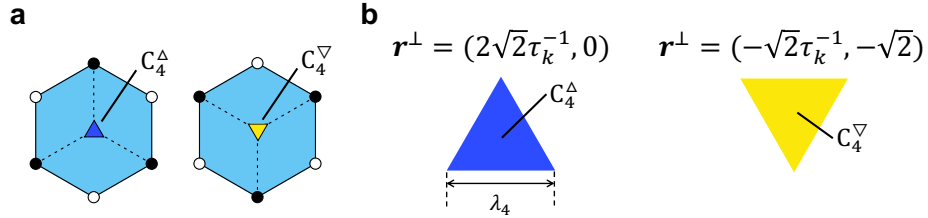
In this section, we consider the decorations on the hexagonal metallic-mean tilings, which should be relevant for the atomic structure of the MC and MD simulations². In a certain parameter regime, MC and MD simulations show the stable solution where the atomic structure is described by large and small hexagons, and parallelograms, as shown in Supplementary Fig. 20. The atomic positions are given in Supplementary Note 8. We find that three atoms are



Supplementary Fig. 20. Atomic structures of the MC and MD simulations. The circles represent the locations of atoms.

located in the vicinity of each vertex in the tilings while the others are located around the center of the L tile.

To clarify how relevant the hexagonal metallic-mean tilings proposed in this study are for the atomic structure observed in MD and MC simulations, we first introduce an auxiliary vertex C_4^Δ (C_4^∇) placed at the center of the L_Δ (L_∇) tile, as shown in Supplementary Fig. 21a. Since the number of the C_4^α ($\alpha = \Delta, \nabla$) vertices corresponds to that



Supplementary Fig. 21. **a** C_4^Δ and C_4^∇ vertices which are defined by dividing L_Δ and L_∇ tiles into three rhombuses. **b** Window of the C_4^Δ (C_4^∇) vertex in the perpendicular space $\mathbf{r}^\perp = (2\sqrt{2}\tau_k^{-1}, 0)$ [$(-\sqrt{2}\tau_k^{-1}, -\sqrt{2})$]. λ_4 is the edge length of the triangles.

of the L_α tiles, its fraction is given as,

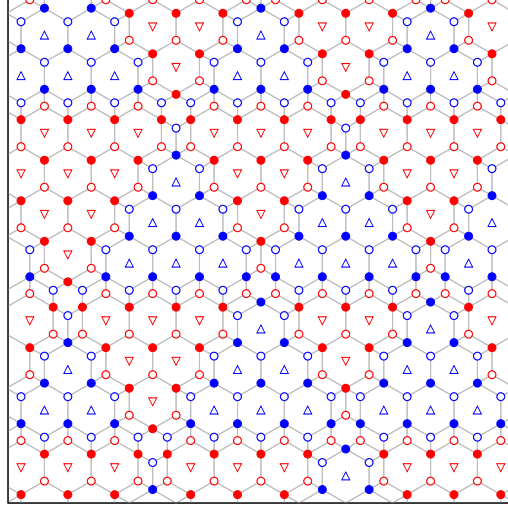
$$f_{C_4^\alpha} = \frac{1}{4} \frac{\tau_k^2}{\tau_k^2 + 3\tau_k + 1}. \quad (51)$$

When the L_α tile is divided into three rhombuses, as shown in Supplementary Fig. 21a, each C_4^α vertex connects to the corner vertices in the B sublattice (the solid circles), and it can be regarded to belong to the A sublattice. Since the distance between the C_4^α and corner vertices corresponds to the longer length ℓ , the set of the six integer indices for the C_4^α vertex is given by

$$\vec{n}_{C_4^\alpha} = \vec{n}_{corner} + \Delta\vec{n}, \quad (52)$$

where \vec{n}_{corner} is the set of the six integer indices for a certain corner vertex in the B sublattice and $\Delta\vec{n} = (n_0, n_1, n_2, 0, 0, 0)^T$ with integer n_m . This means that the C_4^Δ and C_4^∇ vertices are clearly distinguished in the perpendicular space since $y^\perp [= -\sqrt{2}\vec{n}_{C_4^\alpha} \cdot (0, 0, 0, 1, 1, 1)^T]$ for the C_4^α vertices is the same as that for the vertices

belonging to the honeycomb domain with α . Namely, the window for the C_4^Δ (C_4^∇) vertex appears in the perpendicular spaces with $\mathbf{r}^\perp = (2\sqrt{2}\tau_k^{-1}, 0) [(-\sqrt{2}\tau_k^{-1}, -\sqrt{2})]$, as shown in Supplementary Fig. 21b. The edge length of the windows is given by $\lambda_4 = \sqrt{3}$, by taking into account the fraction of the vertices. Supplementary Figure 22 shows the hexagonal bronze-mean tiling with the C_4 vertices, which is obtained by means of the cut-and-projection scheme. We find that the C_4^α auxiliary vertices indeed belong to the honeycomb domain with α . To discuss the spatial structure of the vertices in the perpendicular space in detail, it is useful to consider the corresponding windows in three dimensions ($\hat{x}, \hat{y}, \hat{z} = x^\perp + y^\perp$), as discussed in the main text. Supplementary Figure 23 clarifies that these six windows are the crosssections of the trigonal trapezohedron with the edge length $\sqrt{3}(1 + \tau_k^{-1})$. We find that the vertices in the honeycomb domains with Δ (∇) are located in the upper (lower) windows, which are shown as the blue (red) triangles and hexagon. This is consistent with the fact that certain two windows belonging to the same (different) honeycomb domains are bridged by the vectors $\mathbf{e}_0^h, \mathbf{e}_1^h, \mathbf{e}_2^h$ ($\mathbf{e}_3^h, \mathbf{e}_4^h, \mathbf{e}_5^h$). The middle four windows can be regarded as the crosssections of the regular octahedron, which is shown in Extended Data Fig. 1 in the main text.



Supplementary Fig. 22. Hexagonal bronze-mean tiling with the C_4 vertices. Open (solid) circles at the vertices indicate the sublattice A (B). Open triangles represent the auxiliary C_4 vertices. Blue (red) symbols represent the vertices belonging to the honeycomb domains with Δ (∇).

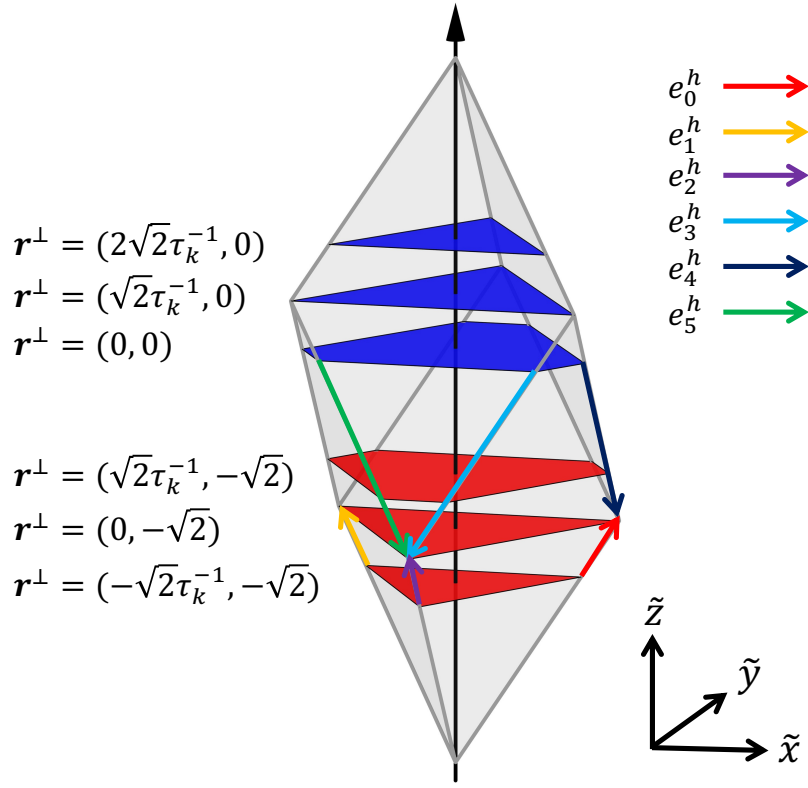
Next, we consider the atomic decorations for the hexagonal metallic-mean tilings. One can divide the atoms into three groups with $\alpha (= \Delta, \nabla)$, as shown in Supplementary Fig. 24. The group u_1^α is composed of the atoms around the vertex in the hexagonal metallic-mean tiling and the group u_2^α is composed of the atoms around the auxiliary vertex C_4^α (the center of L_α tiles). The other group v^α are located in the L_α tile, but far from the center.

Now, we would like to describe the atomic structures, specifying the sets of the six indices for these atoms. First, we focus on certain atoms in the groups u_1^Δ and u_1^∇ around the vertex X^Δ and X^∇ , which are pointed in Supplementary Figs. 24a and b, respectively. We find that the atom with $\alpha = \Delta$ (∇) is located in the backward (forward) direction of the vectors \mathbf{e}_0 from X^Δ (X^∇). Since the atoms also belong to the honeycomb domain with α , the sets of the six indices \vec{n}_{atom} for these atoms are given as

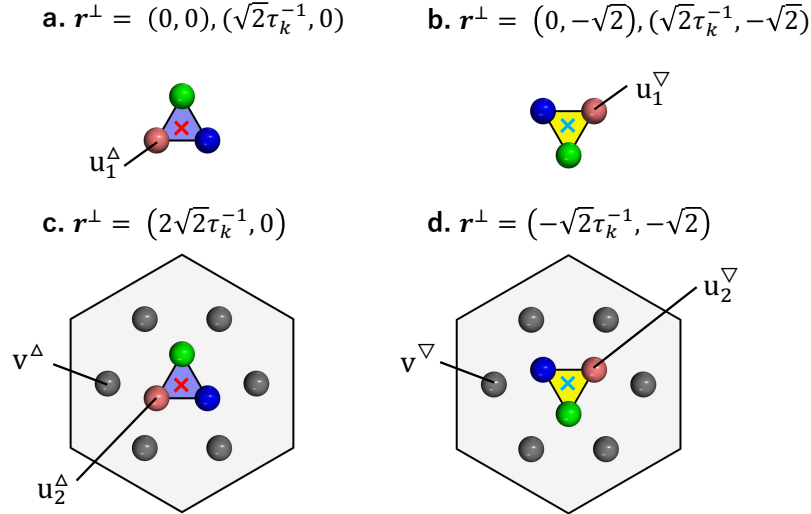
$$\vec{n}_{\text{atom}} = \vec{n}_{X^\alpha} + \vec{n}, \quad (53)$$

$$\vec{n} = (\mp c, 0, 0, 0, 0, 0)^T, \quad (54)$$

where \vec{n}_{X^α} is the set of the six integer indices for the X^α vertex, and the above (under) sign corresponds to $\alpha = \Delta$ (∇). In the perpendicular space \mathcal{S} , the window of the corresponding atoms appears $\vec{\mathbf{d}}$ away from the window of X^α , where $\vec{\mathbf{d}} = \mp c\tilde{\mathbf{e}}_0$. Examining the positions for the atoms of the u_1^α , u_2^α , and v^α groups, we determine the sets of the six indices, which are explicitly shown in Supplementary Table 3. Supplementary Figure 25a (b) shows the windows for the groups u_1^Δ, u_2^Δ (u_1^∇, u_2^∇) in the perpendicular spaces. Supplementary Figure 26a (b) shows the windows for the group v^Δ (v^∇) in the perpendicular space with $\mathbf{r}^\perp = (2\sqrt{2}\tau_k^{-1}, 0) [(-\sqrt{2}\tau_k^{-1}, -\sqrt{2})]$. We generate the hexagonal metallic-mean tilings with the atomic decorations by the cut-and-project scheme, which are schematically shown in Supplementary Fig. 27.



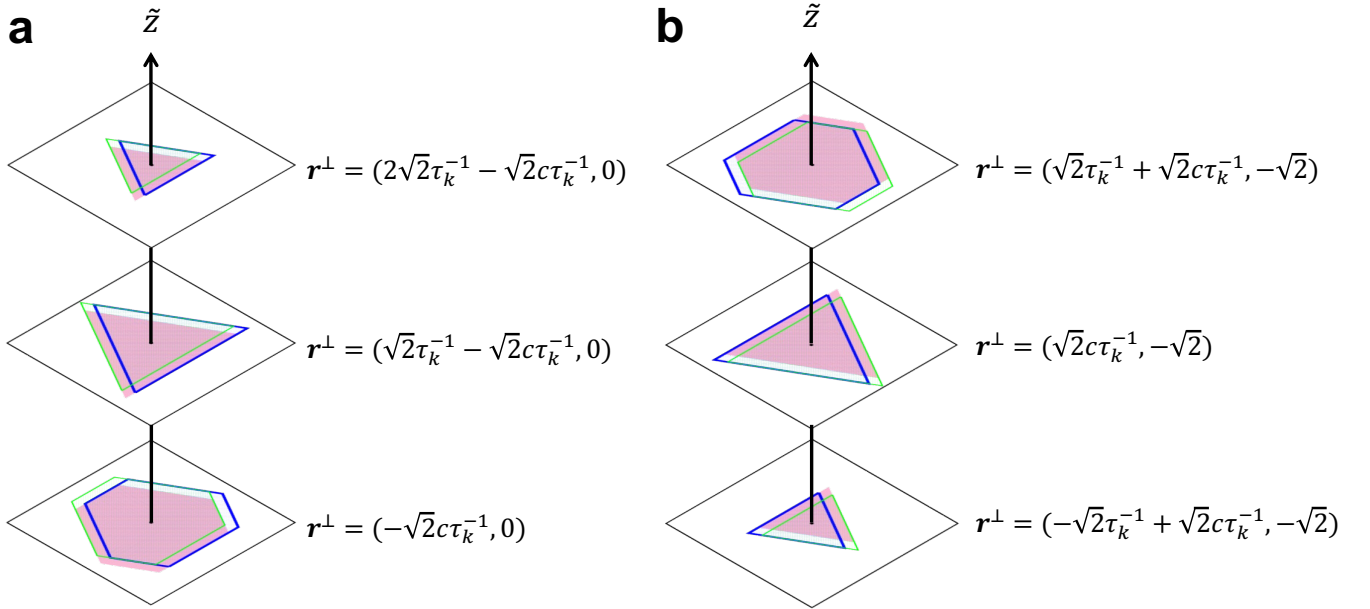
Supplementary Fig. 23. The perpendicular space $[\mathbf{r}^\perp = (2\sqrt{2}\tau_k^{-1}, 0), (\sqrt{2}\tau_k^{-1}, 0), (0, 0), (\sqrt{2}\tau_k^{-1}, -\sqrt{2}), (0, -\sqrt{2}), (-\sqrt{2}\tau_k^{-1}, -\sqrt{2})]$ of the hexagonal bronze-mean tiling with $k = 3$ in three dimensions with $(\tilde{x}, \tilde{y}, \tilde{z} = x^\perp + y^\perp)$. The colored arrows indicate the projected basis vectors \mathbf{e}_i^h and the blue (red) triangles and hexagon indicate the windows for the honeycomb domains with \triangle (∇).



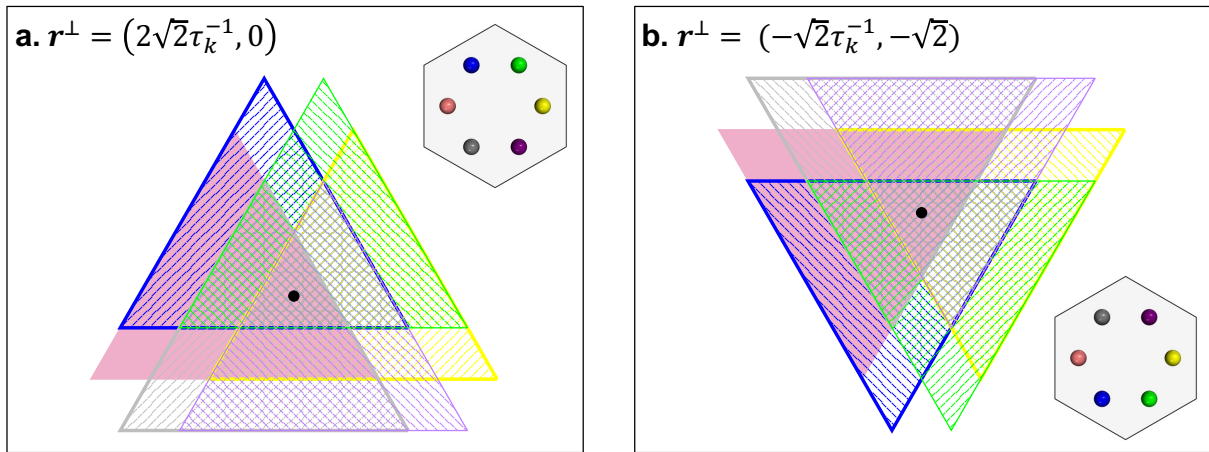
Supplementary Fig. 24. Positions of atoms in the decorated tiling. Blue, green, and red circles represent three kinds of the atoms in the \mathbf{u}_1 and \mathbf{u}_2 groups and gray circles represent the atoms in the \mathbf{v} group. **a** (**b**) Red (blue) cross represents the vertex in the honeycomb domain with \triangle (∇), which is mapped to the perpendicular space in $\mathbf{r}^\perp = (0, 0), (\sqrt{2}\tau_k^{-1}, 0)$ [$(0, -\sqrt{2}), (\sqrt{2}\tau_k^{-1}, -\sqrt{2})$]. **c** (**d**) Atomic decorations of the L_\triangle (L_∇) tile. Red (blue) cross represents the auxiliary C_4^\triangle (C_4^∇) vertex, which is mapped to the perpendicular space in $\mathbf{r}^\perp = (2\sqrt{2}\tau_k^{-1}, 0)$ [$(-\sqrt{2}\tau_k^{-1}, -\sqrt{2})$].

Group	\mathbf{r}^\perp	Window	$3\tilde{\mathbf{n}}^T$
\mathbf{u}_1^Δ	$(-\sqrt{2}c\tau_k^{-1}, 0), (\sqrt{2}\tau_k^{-1} - \sqrt{2}c\tau_k^{-1}, 0)$	Hexagon	$(\mp 3c, 0, 0, 0, 0, 0)$
\mathbf{u}_1^∇	$(\sqrt{2}c\tau_k^{-1}, -\sqrt{2}), (\sqrt{2}\tau_k^{-1} + \sqrt{2}c\tau_k^{-1}, -\sqrt{2})$		$(0, \mp 3c, 0, 0, 0, 0)$
\mathbf{u}_2^Δ	$(2\sqrt{2}\tau_k^{-1} - \sqrt{2}c\tau_k^{-1}, 0)$	Triangle	$(0, 0, \mp 3c, 0, 0, 0)$
\mathbf{u}_2^∇	$(-\sqrt{2}\tau_k^{-1} + \sqrt{2}c\tau_k^{-1}, -\sqrt{2})$		
\mathbf{v}^Δ	$(2\sqrt{2}\tau_k^{-1}, 0)$	Triangle	$(-1, 1, 0, 0, 0, 0)$
\mathbf{v}^∇	$(-\sqrt{2}\tau_k^{-1}, -\sqrt{2})$		$(1, -1, 0, 0, 0, 0)$
			$(-1, 0, 1, 0, 0, 0)$
			$(1, 0, -1, 0, 0, 0)$
			$(0, -1, 1, 0, 0, 0)$
			$(0, 1, -1, 0, 0, 0)$

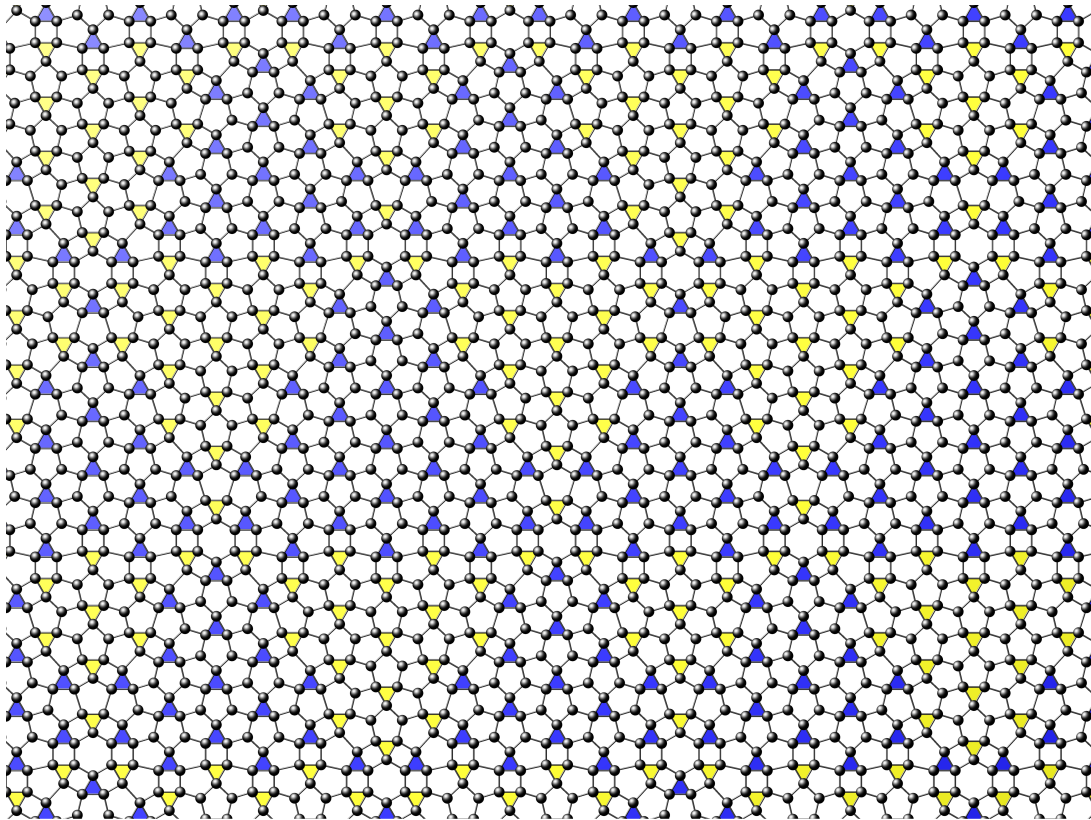
Supplementary Table 3. Occupied plane \mathbf{r}^\perp and corresponding window shape in the perpendicular space. Three sets of six indices for the \mathbf{u}_1 and \mathbf{u}_2 groups are given, where the above (under) sign corresponds to Δ (∇). Six sets of six indices for the \mathbf{v} group are also given. $c = (\sqrt{33} - 3)/12 = 0.2287$.



Supplementary Fig. 25. **a** (**b**) Windows for the $\mathbf{u}_1^\Delta, \mathbf{u}_2^\Delta$ ($\mathbf{u}_1^\nabla, \mathbf{u}_2^\nabla$) groups in the perpendicular spaces for the hexagonal golden-mean tiling with $k = 1$. Each layer has three distinct windows, whose colors correspond to the colors for the atom shown in Supplementary Fig. 24.



Supplementary Fig. 26. Windows for the v^Δ and v^∇ groups in the perpendicular spaces with **a** $r^\perp = (2\sqrt{2}\tau_k^{-1}, 0)$ and **b** $(-\sqrt{2}\tau_k^{-1}, -\sqrt{2})$ for the hexagonal golden-mean tiling with $k = 1$, respectively. Insets show the positions of atoms in the v group. Each layer has six distinct triangular windows, whose colors correspond to the colors of the atoms shown in the inset.



Supplementary Fig. 27. Decorated hexagonal silver-mean tilings.

We calculate the lattice structure factors of the decorated tilings, extending the method shown in Supplementary Note 7. The atoms in the decorated tiling are divided into three groups u_1 , u_2 , and v , as shown in Supplementary Fig. 24. The density of the atoms is then given as

$$\rho(\mathbf{r}) = \rho_{u_1}(\mathbf{r}) + \rho_{u_2}(\mathbf{r}) + \rho_v(\mathbf{r}), \quad (55)$$

$$\begin{aligned} \rho_{u_1}(\mathbf{r}) = & \sum_{n=0}^2 \left[\left(\sum_{j \in (0,0)^\perp} + \sum_{j \in (1,0)^\perp} \right) \delta(\mathbf{r}_j - c\mathbf{e}_n - \mathbf{r}) \right] \\ & + \sum_{n=0}^2 \left[\left(\sum_{j \in (0,1)^\perp} + \sum_{j \in (1,1)^\perp} \right) \delta(\mathbf{r}_j + \mathbf{e}_n - \mathbf{r}) \right], \end{aligned} \quad (56)$$

$$\rho_{u_2}(\mathbf{r}) = \sum_{n=0}^2 \left[\sum_{j \in (2,0)^\perp} \delta(\mathbf{r}_j - c\mathbf{e}_n - \mathbf{r}) \right] + \sum_{n=0}^2 \left[\sum_{j \in (-1,1)^\perp} \delta(\mathbf{r}_j + c\mathbf{e}_n - \mathbf{r}) \right], \quad (57)$$

$$\rho_v(\mathbf{r}) = \sum_{n=0}^5 \left[\left(\sum_{j \in (2,0)^\perp} + \sum_{j \in (-1,1)^\perp} \right) \delta \left(\mathbf{r}_j + R^n \left\{ \frac{\mathbf{e}_1 - \mathbf{e}_0}{3} \right\} - \mathbf{r} \right) \right], \quad (58)$$

where \mathbf{r}_i represents the position of the vertex site in the tiling and the operator R rotates the vectors by the angle $\pi/3$, as

$$R = \begin{pmatrix} \cos(\pi/3) & -\sin(\pi/3) \\ \sin(\pi/3) & \cos(\pi/3) \end{pmatrix}. \quad (59)$$

The operation is represented as $R\mathbf{e}_i = -\mathbf{e}_j$ ($i = 0, 1, 2$), where $j = i - 1 + 3\delta_{0i}$. We have used the position of atoms, which are explicitly shown in Supplementary Table 3. In the lattice structure factors, the peak positions are represented as $\mathbf{q} = \sum_{m=0}^5 \tilde{n}_m \mathbf{q}_m$, where \tilde{n}_m is an integer and \mathbf{q}_m is the reciprocal vector derived in Supplementary Note 5. The Fourier transform of the density $\rho(\mathbf{q}) = \int \rho(\mathbf{r}) \exp(-i\mathbf{r} \cdot \mathbf{q}) d\mathbf{r}$ can be represented in terms of the Fourier transform of the occupation domains \mathcal{F}_{mn} as,

$$\begin{aligned} \rho(\mathbf{q}) = & \exp(-i\sqrt{2}c\tau_k^{-1}q_0^\perp) \sum_{n=0}^2 \exp(-ic\tilde{\mathbf{e}}_n \cdot \tilde{\mathbf{q}}) \left[\mathcal{F}_{00}(\tilde{\mathbf{q}}) + \exp(i\sqrt{2}\tau_k^{-1}q_0^\perp) \mathcal{F}_{10}(\tilde{\mathbf{q}}) + \exp(i2\sqrt{2}\tau_k^{-1}q_0^\perp) \mathcal{F}_{20}(\tilde{\mathbf{q}}) \right] \\ & + \exp(i\sqrt{2}c\tau_k^{-1}q_0^\perp) \sum_{n=0}^2 \exp(ic\tilde{\mathbf{e}}_n \cdot \tilde{\mathbf{q}}) \exp(-i\sqrt{2}q_1^\perp) \left[\mathcal{F}_{01}(\tilde{\mathbf{q}}) + \exp(i\sqrt{2}\tau_k^{-1}q_0^\perp) \mathcal{F}_{11}(\tilde{\mathbf{q}}) + \exp(-i\sqrt{2}\tau_k^{-1}q_0^\perp) \mathcal{F}_{-11}(\tilde{\mathbf{q}}) \right] \\ & + \sum_{n=0}^5 \exp \left(iR^n \left\{ \frac{\tilde{\mathbf{e}}_1 - \tilde{\mathbf{e}}_0}{3} \right\} \cdot \tilde{\mathbf{q}} \right) \left[\exp(i2\sqrt{2}\tau_k^{-1}q_0^\perp) \mathcal{F}_{20}(\tilde{\mathbf{q}}) + \exp(-i\sqrt{2}\tau_k^{-1}q_0^\perp) \exp(-i\sqrt{2}q_1^\perp) \mathcal{F}_{-11}(\tilde{\mathbf{q}}) \right]. \end{aligned} \quad (60)$$

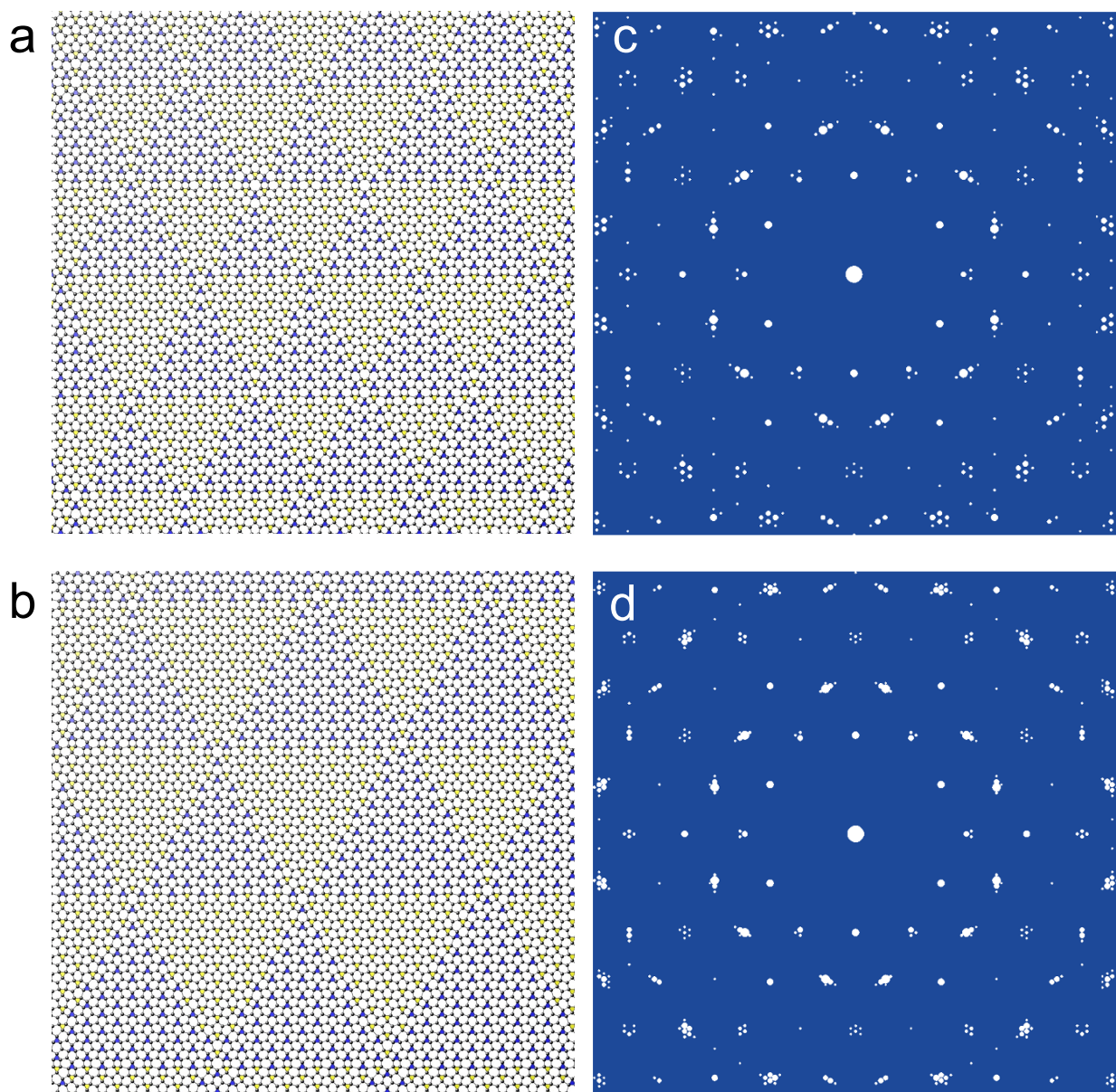
Then, we obtain the lattice structure factors $|\rho(\mathbf{q})|^2$.

Supplementary Figure 28 shows the decorated tilings and the corresponding lattice structure factors for $k = 3$ and $k = 5$. We confirm that the peak structures of the decorated tilings are in a good agreement with the MC results shown in Supplementary Fig. 19.

¹ S. Coates, A. Koga, T. Matsubara, R. Tamura, H. R. Sharma, R. McGrath, and R. Lifshitz, ‘‘Hexagonal and trigonal quasiperiodic tilings,’’ (2023), arXiv:2201.11848 [cond-mat.soft].

² M. Engel, Phys. Rev. Lett. **106**, 095504 (2011).

³ M. Engel and H.-R. Trebin, Phys. Rev. Lett. **98**, 225505 (2007).



Supplementary Fig. 28. The decorated tilings (**a**, $k = 3$ and **b**, $k = 5$) and the lattice structure factors (**c**, $k = 3$ and **d**, $k = 5$). The area is proportional to the intensity.